JOHANN WOLFGANG GOETHE
UNIVERSITÄT
FRANKFURT AM MAIN

Probing Self-Interacting Dark Matter with the GD-1 Stellar Stream

Masterarbeit

zur Erlangung des akademischen Grades
Master of Science in Physik
am Institut für Theoretische Physik
der Goethe-Universität in Frankfurt am Main

vorgelegt von

Alexander Huhn

eingereicht am 7. August 2025

Erstgutachterin: Prof. Dr. Laura Sagunski
Zweitgutachter: Prof. Dr. Jürgen Schaffner-Bielich

Abstract

In this work, different dark matter models, Cold Dark Matter, Self-Interacting Dark Matter, and Dissipative Self-Interacting Dark Matter, were tested using the GD-1 stellar stream by generating and analyzing the respective density power spectra. GD-1 is particularly well suited for this purpose due to the availability of high-precision observational data and its clearly defined density profile. Notably, GD-1 features a gap whose structure possibly suggests a perturbation by a massive and compact object, potentially a dark matter subhalo. To investigate this possibility, subhalo impacts were simulated for each of the models, and the resulting density power spectra were computed as a function of the angular coordinate ϕ_1 and the path length s. The results show no significant differences between the models. This may indicate that the power spectrum is not the most suitable tool to accurately resolve small-scale density fluctuations such as those caused by a subhalo impact.

Zusammenfassung

In dieser Arbeit wurden verschiedene dunkle Materie Modelle, Cold Dark Matter, Self-interacting Dark Matter und Dissipative Self-Interacting Dark Matter mit Hilfe des GD-1 Stellar Streams getestet, indem jeweils ein Power Spectrum erstellt wurde. GD-1 ist aufgrund sehr präziser Beobachtungsdaten und einem sehr ausgeprägten Dichteprofil hierfür besonders geeignet und weist eine Lücke auf, deren Struktur möglicherweise darauf hindeutet, dass sie von einem massiven und kompakten Objekt stammen könnte, wobei viel dafür spricht, dass dafür ein dunkle Materie Subhalo in Betracht kommen könnte. Dazu werden zunächst Subhalo Impacts für die verschiedenen Modelle simuliert und anschließend Density Power Spectra als Funktion von ϕ_1 und der path length s erstellt. Im Ergebnis ist kein wesentlicher Unterschied zwischen den Modellen erkennbar. Möglicherweise stellt ein Power Spectrum kein optimales Mittel dar, um Dichtefluktuationen auf kleinen Skalen, wie sie nach einem Subhalo Impact auftreten, präzise abzubilden.

Selbstständigkeitserklärung

Hiermit erkläre ich, dass ich die Arbeit selbstständig und ohne Benutzung anderer als der angegebenen Quellen und Hilfsmittel verfasst habe. Alle Stellen der Arbeit, die wörtlich oder sinngemäß aus Veröffentlichungen oder aus anderen fremden Texten entnommen wurden, sind von mir als solche kenntlich gemacht worden. Ferner erkläre ich, dass die Arbeit nicht - auch nichts auszugsweise - für eine andere Prüfung verwendet wurde.

Frankfurt, den 7. August 2025

_____

Alexander Huhn

Notation

Abbreviations

Abbreviation	*Meaning*
CMB	Cosmic Microwave Background
CSD	Cross Spectral Density
DFT	Discrete Fourier Transform
DG	Dwarf Galaxy
DM	Dark Matter
DSIDM	Dissipative Self-interacting Dark Matter
FLRW	Friedmann-Lemaître-Robertson-Walker metric
GC	Globular Cluster
GD-1	Grillmair–Dionatos 1 stream
HDM	Hot Dark Matter
NFW	Navarro-Frenk-White profile
MC	Molecular Cloud
MPI	Message Passing Interface
MW	Milky Way
PSD	Power Spectral Density
SDSS	Sloan Digital Sky Survey
SIDM	Self-interacting Dark Matter
WDM	Warm Dark Matter

Symbols and Units

Symbol/Unit	*Meaning*
s (time)	second
h	hour
d	day
a	year (cosmological)
y	year (astrophysical)
ly	light-year
pc	parsec
$M_\odot$	solar mass
s (path)	proper path length along GD-1
D	heliocentric distance to GD-1
c	speed of light in vacuum
G	Newton's gravitational constant
H	Hubble constant

Contents

Chapter 1

Introduction

1.1 The Visible and the Invisible

> *"So remember to look up at the stars and not down at your feet. Try to make sense of what you see and hold on to that childlike wonder about what makes the universe exist."*
>
> – Stephen Hawking

In his *Allegory of the Cave*, the Greek philosopher *Plato* describes people who have been chained in a dark cave since birth, such that they can only look at the wall in front of them. Behind them burns a fire, and between the fire and the prisoners, objects are moved, casting shadows onto the cave wall. The prisoners perceive these shadows as the only reality. When some of them are freed and leave the cave, they come to recognize the true world outside. They see the earth, the sun, and at night the whole cosmos stretching above them with its beauty and understand that the shadows were merely illusions. A parallel between Plato's allegory and our understanding of the universe has been drawn, for example in the context of the film *Interstellar* in which the former NASA pilot Cooper joins an expedition that travels through a wormhole to explore new worlds and ultimately save humanity [81]. But it can also serve as metaphor for our general understanding of the universe and particularly the mystery of *Dark Matter* (DM). If, as it seems to be the case, 85% of all matter in the universe [126] consists of this substance we do not yet understand, then what we can observe today is, metaphorically speaking, merely a shadow on the wall of the cave. And despite decades of effort to break free, no one has truly left the cave yet. But what we can do is study the shadows in detail and analyze the traces that this mysterious form of matter leaves behind. One such trace is the stellar stream *GD-1* [45], a long, thin structure of stars stretching across several kiloparsecs in the halo of the *Milky Way* (MW). Within this stream lies a gap whose shape and properties suggest it may have been caused by a collision with a DM subhalo. It is, in a sense, a direct shadow cast by dark matter into our cave, that might help us find a path into the open. This thesis attempts to examine that shadow, that may one day take on tangible form under the open starry sky of reality.

FIGURE 1.1: Artistic illustration of a *wormhole* [91], a theoretical concept from general relativity that describes a shortcut between two distant points through spacetime, like a tunnel. In the film Interstellar, NASA pilot Cooper travels through such a wormhole to save humanity. Plato's *Allegory of the Cave* has been interpreted as a metaphor for this film [81]. This interpretation can also be applied to *Dark Matter*, a mystery that science has been puzzling over for several decades (M. A. Garlick/ESO/CC BY-SA 4.0) [58].

1.2 Motivation

Among the stellar streams in the *MW*, *GD-1* is particularly well observed and exhibits a clearly defined density profile. One of its gaps shows a structure that could be the result of a collision with a DM subhalo. In the ΛCDM model, dark matter halos play a major role, forming the framework within which baryonic matter first assembled. During the process of accretion, these halos orbit as subhalos around main halos that surround galaxies such as the MW. The precise structure of one gap in GD-1, which might have formed as a consequence of such a collision, would be related to the density profile of this subhalo. This profile depends on the DM model considered and can be either cored, cuspy or super-cuspy. This allows conclusions to be drawn about the structure of DM. A useful tool to describe structures and patterns in astrophysical objects is the so-called power spectrum. In this work, this is calculated and interpreted for all three models using a specially developed code.

Chapter 2

Theory

2.1 Cosmological and Astrophysical Background

2.1.1 The ΛCDM Model

2.1.1.1 Cosmological Framework

The particle models examined in this thesis are based on the framework of *Cold Dark Matter* (CDM) [43, 121]. Together with *Dark Energy* Λ [102], CDM is a part of the ΛCDM model. This is the standard model of cosmology, describing both the large-scale structure and the evolution of our universe. It is based on the *cosmological principle*, which states that the universe is *homogeneous* (uniformly distributed) and *isotropic* (the same in all directions) on large scales. In such a universe, distances can be described using the Friedmann-Lemaître-Robertson-Walker (FLRW) metric [133]

$$ds^2 = -c^2dt^2 + a(t)^2\left[\frac{dr^2}{1-kr^2} + r^2(d\theta^2 + \sin^2\theta d\phi^2)\right] \tag{2.1}$$

with the scale factor $a(t)$, describing the expansion of the universe, the radial distance r, representing the distance in a specific coordinate system, the curvature parameter k, characterizing the spatial curvature of the universe[1], and the speed of light c. The Friedmann equations are derived from the Einstein field equations

$$R_{\mu\nu} - \frac{1}{2}g_{\mu\nu}R + g_{\mu\nu}\Lambda = \frac{8\pi G}{c^4}T_{\mu\nu} \tag{2.2}$$

with the Ricci curvature tensor $R_{\mu\nu}$, the metric tensor $g_{\mu\nu}$, the Ricci scalar R, the cosmological constant Λ, the energy-momentum-tensor $T_{\mu\nu}$, and Newton's gravitational constant G. If the matter is isotropically distributed, $T_{\mu\nu}$ can be expressed as

[1] The universe can be open ($k = -1$), flat ($k = 0$) or closed ($k = 1$).

$$T_{\mu\nu} = \begin{pmatrix} -\rho c^2 & 0 & 0 & 0 \\ 0 & p & 0 & 0 \\ 0 & 0 & p & 0 \\ 0 & 0 & 0 & p \end{pmatrix} \tag{2.3}$$

By inserting the FLRW metric (Eq. 2.1) into the Einstein field equations (Eq. 2.2), one obtains the Friedmann equations

$$H^2 = \left(\frac{\dot{a}}{a}\right)^2 = \frac{8\pi G}{3}\rho - \frac{kc^2}{a^2} + \frac{\Lambda c^2}{3} \tag{2.4a}$$

$$\frac{\ddot{a}}{a} = -\frac{4\pi G}{3}\left(\rho + \frac{3p}{c^2}\right) + \frac{\Lambda c^2}{3} \tag{2.4b}$$

with the Hubble parameter H, the total density ρ and the total pressure p. The equation of state describes the relationship between the pressure p and the energy density ρ_i of a given component in the universe. It is defined as

$$\rho_i = \rho_{i,0}\left(\frac{a_0}{a}\right)^{3(1+w_i)} \tag{2.5}$$

where w_i are the equation-of-state parameters and $\rho_{i,0}$ the present-day energy density of the component i. The components of the universe in the ΛCDM model are baryonic and (cold) *dark matter* (DM) (m), radiation (r), and dark energy (Λ). Dark energy (Λ) acts as a repulsive force that counteracts gravity on cosmological scales, driving the accelerated expansion of the universe. The critical density ρ_{crit}, at which the universe is exactly flat ($k = 0$), is defined as

$$\rho_{crit} = \frac{3H_0^2}{8\pi G} \tag{2.6}$$

Dividing the first Friedmann equation (Eq. 2.4a) by H_0 then yields

$$\frac{H^2}{H_0^2} = \sum_i \Omega_{i,0}\left(\frac{a_0}{a}\right)^{3(1+w_i)} \tag{2.7}$$

where H_0 is the Hubble constant today. The equation-of-state parameters w_i are defined as the relation between pressure and density ($w_i = p_i/\rho_i$) and have the values $w_m = 0$ (matter), $w_r = 1/3$ (radiation) and $w_\Lambda = -1$ (dark energy). Equation (2.7) can then be rewritten as

$$\frac{H^2}{H_0^2} = \sum_i \Omega_{i,0}\left(\frac{a_0}{a}\right)^{3(1+w_i)} = \underbrace{\Omega_{r,0}\left(\frac{a_0}{a}\right)^4}_{\text{radiation}} + \underbrace{\Omega_{m,0}\left(\frac{a_0}{a}\right)^3}_{\text{matter}} + \underbrace{\Omega_{\Lambda,0}}_{\text{dark energy}} \tag{2.8}$$

where matter can be both baryonic and collisionless CDM. a is the scale factor of the universe and describes how much the universe has expanded or contracted relative to a specific reference time. a_0 is defined as the scale factor today, so that today $a = a_0$. With the *density parameters* (cosmological parameters) Ω_i, defined as

$$\Omega_i = \frac{\rho_i}{\rho_{crit}} \tag{2.9}$$

it is now possible to express each component of the universe relative to the critical density ρ_{crit} (Eq. 2.6)

$$\Omega_{tot} = \sum_i \Omega_i = \Omega_r + \Omega_m + \Omega_\Lambda \tag{2.10}$$

where Ω_{tot} is the total density parameter of the universe.

2.1.1.2 Composition of the Universe

Ω_{tot} (Eq. 3.13, see Subsubsec. ▶ 2.1.1.1) describes the contribution of all the individual components of the universe. Modified particle models in the framework of CDM need to be in accordance with the structure formation of the universe (see Subsubsec. ▶ 2.1.2.1). For example, the density parameters Ω_i determine how quickly matter collapses and how dark matter interacts with itself and other components which is relevant for the self-interactions in *Self-interacting Dark Matter* (SIDM). To determine the composition of the universe, the *Cosmic Microwave Background* (CMB) (Figure A.1) can be used [51] (for a description of the single steps, see ▶ A.1). Table (2.1) shows the composition of the present-day universe, as determined by the latest measurements [126]. Figure (2.1) illustrates the evolution of the universe's composition from the time of recombination to the present day.

Parameter	*Value*	$\pm 1\sigma$
Ω_m (matter)	0.3153	0.0073
Ω_Λ (dark energy)	0.6847	0.0073
$\Omega_b h^2$ (baryons)	0.02237	0.00015
$\Omega_c h^2$ (cold dark matter)	0.1200	0.0012
Ω_r (radiation)	$\approx 5 \times 10^{-5}$	-

TABLE 2.1: Cosmological parameter Ω_i with their values and uncertainties. The values are taken from [126].

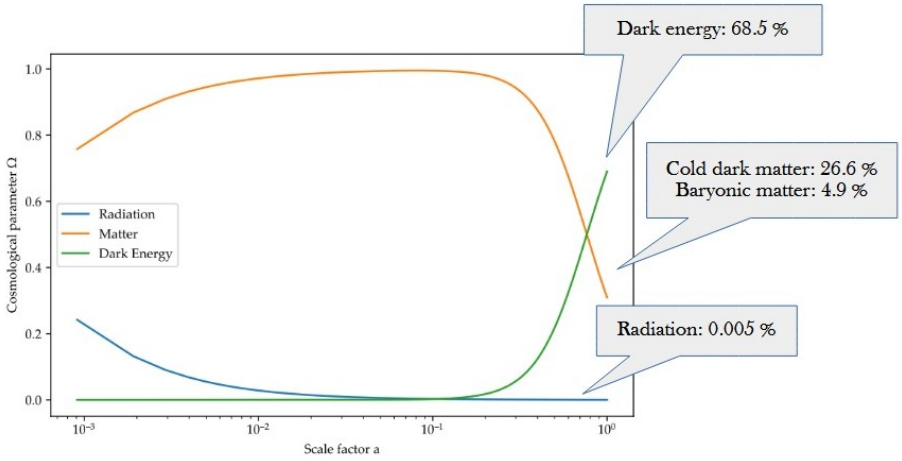

FIGURE 2.1: Composition of the universe from the *recombination* until today. In this figure, the energy density ρ_i for each component i has been determined using Equation (2.5), where $\rho_{i,0}$ denotes the present-day energy density, obtained from the CMB as described in the preceding section. The cosmological parameters Ω_i were then calculated using Equation (2.9).

2.1.2 Structure Formation

2.1.2.1 Dark Matter in the Context of the Cosmic Evolution

Epoch	Time after Big Bang	Temperature
Planck Era	< 10^{-43} s	> 10^{19} GeV
GUT Era	10^{-43} – 10^{-36} s	10^{15} – 10^{19} GeV
Inflation and Reheating	10^{-36} – 10^{-32} s	Model dependent
Electroweak Era	10^{-12} – 10^{-6} s	100 GeV – 1 TeV
Quark-Gluon-Plasma	10^{-6} – 10^{-4}	100 MeV – 1 GeV
Hadron Era	10^{-4} – ca. 1 s	ca. 100 MeV
Lepton Era	1 – 10 s	ca. 1 MeV
Photon Era	10 s – 380,000 a	< MeV – ca. 0.3 eV
Recombination	ca. 380,000 a	ca. 0.3 eV
Dark Ages	380,000 – 150 M a	0.3 eV – 1 meV
Reonization	ca. 150 M – 1 T a	ca. 1 eV
Present Day	13.8 T a	ca. 2.7 K

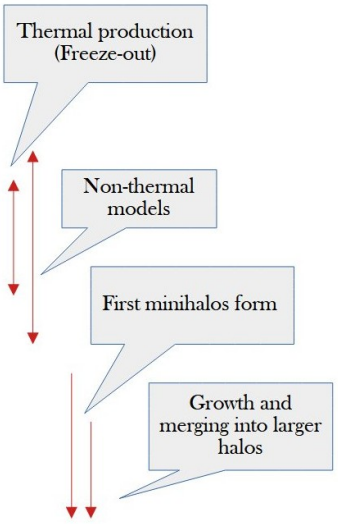

FIGURE 2.2: Epochs of the universe, as well as the developmental phases of DM. Recombination marks the moment when the universe became transparent and simultaneously the beginning of structure formation [124].

Now that the *constituents* of the universe [80] have been identified, the question arises as to how its *structure* could have formed, ranging from *galactic structures* (such as stars, star clusters, and galaxies) to the *cosmic web* (filaments, voids, and nodes) [106]. Figure (2.2) shows the evolution of DM within the framework of the various cosmic epochs. This is relevant to understand the abundance of *DM subhalos* in the *Milky Way* (MW), which are a natural consequence of the structure formation in the universe. According to the standard description provided by the ΛCDM model, this formation proceeds hierarchically, from smaller to larger structures (in contrast to, for example, the top-down scenario of hot DM models) [47]. As shown in Figure (2.2), DM is produced at different stages of cosmic evolution depending on the model (whether through *freeze out* [79], the standard mechanism, or alternative *non thermal* explanations). However, in all cases, its production is complete by the time of recombination. This is also the point at which structure formation begins. DM plays an important role in this process [47]. Since it does not interact electromagnetically, it can collapse early under gravity and thus drives the formation of structures. Small density fluctuations initially lead to the formation of small halos, which merge over time through hierarchical accretion into larger structures. Baryonic matter cools down and subsequently falls into the already existing dark matter halos. These halos connect to form filaments, nodes, and voids, known collectively as the *cosmic web*. Thus, DM forms the gravitational backbone that governs the motion of galaxies and larger structures [120].

2.1.2.2 The Accretion of Subhalos

Due to hierarchical structure formation, the universe today still hosts a large population of DM halos of various sizes [92]. If smaller halos come close to the sphere of a big DM halo, hosting a galaxy such as the MW, it can become gravitationally bound and turn into a *subhalo*. Figure (2.3) shows this process, called *accretion*. Since numerous of such subhalos are located within the halo of the MW, collisions with stellar streams are a realistic scenario, one of which may have caused the a in GD-1 that forms the basis of this analysis. In the MW there are $10^4 - 10^5$ such subhalos with masses greater than $10^5 M_\odot$ [119]. If the subhalo crosses the *virial radius* of the host halo (*Step 1*, see Fig. 2.3), $r_{infall} \leq R_{vir}$, with r_{infall} defined as the distance from the center of the host halo to the subhalo at the moment it crosses the host's virial radius, it becomes gravitationally bound. The virial radius R_{vir} [31] is defined as

$$R_{vir} = \left(\frac{3M_{vir}}{4\pi \Delta_c \rho_{crit}} \right)^{1/3} \tag{2.11}$$

with the overdensity factor Δ_c, which describes how much denser a halo is compared to

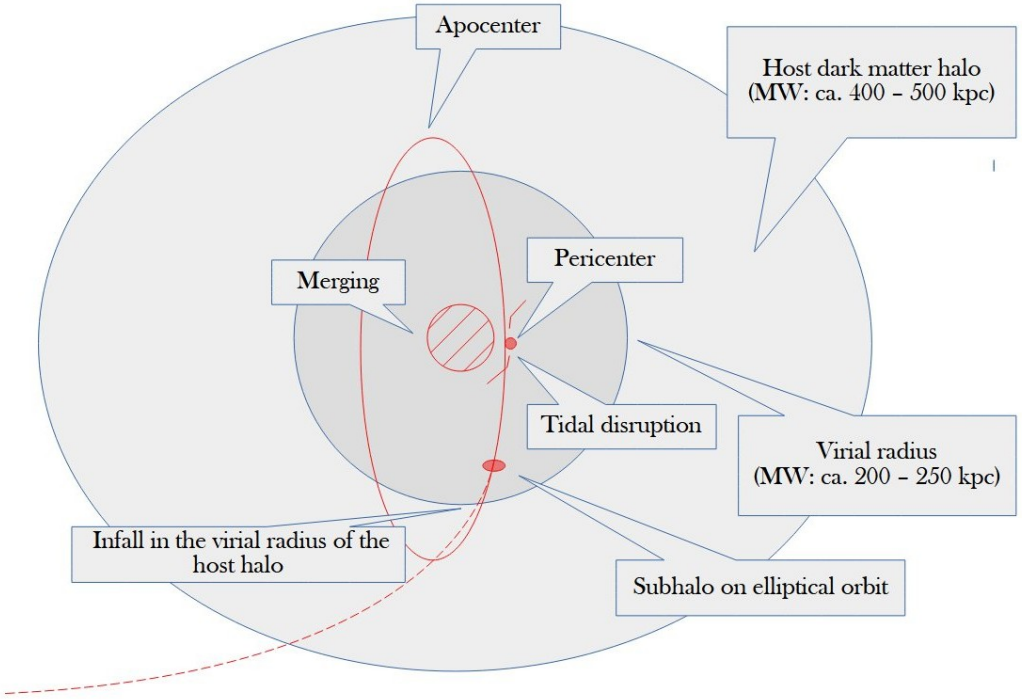

FIGURE 2.3: Illustration of the different steps in the accretion of subhalos: *Virial crossing* (*Step 1*), *tidal stripping* and *dynamical friction* during the (usually) eccentric orbit (*Step 2*), and *merging or tidal disruption* when the subhalo has reached the center of the host halo (*Step 3*).

the average critical density of the universe[2] and ρ_{crit} the critical density [101], defined for a flat universe as

$$\rho_{crit} = \frac{3H^2}{8\pi G} \tag{2.12}$$

When the smaller halo has become gravitationally bound to the host halo, it usually moves on (usually eccentric, sometimes even strongly elongated) orbits around the center (*Step 2*). The closest point to the center of the host halo is called *pericenter*, the most distant *apocenter*. During this orbit, two processes can take place. The first, *tidal stripping*, means, that DM is *stripped away* from the subhalo, caused by the tidal forces[3]. While within tidal radius [15]

$$r_t \approx R\left(\frac{m_{sub}}{3M(R)}\right)^{1/3} \tag{2.13}$$

[2] A typical value would be $\Delta_c = 200$ [31].

[3] That means that the gravitational force acts with different strength on different parts of the smaller object. It is the same force, that the moon exhibits on the ocean waters, causing tides.

the gravitational pull of the subhalo dominates, outside the tidal forces on its particles dominate. R is the distance of the subhalo to the center of the main halo, m_{sub} the mass of the subhalo and $M(R)$ the mass of the main halo within R. Once, enough DM has been stripped from the subhalo, the baryonic matter (forming a Dwarf Galaxy (DG)), typically located deeper in the gravitational potential, can also be removed by tidal forces[4]. The second process is called *dynamical friction* and occurs, when the subhalo moves through a background particle field (as it can be the DM of the host halo). The gravitational force of the subhalo then attracts the DM around it, creating an overdensity behind it. This gravitational action slows down the subhalo and is called dynamical friction. It can be described by the Chandrasekhar formula [37]

$$\frac{d\vec{v}}{dt} = -\frac{4\pi G^2 m\rho \ln\Lambda}{v^3}\left[\mathrm{erf}\left(\frac{v}{\sqrt{2}\sigma}\right) - \frac{2v}{\sqrt{\pi}\sqrt{2}\sigma}e^{-\frac{v^2}{2\sigma^2}}\right]\vec{v} \tag{2.14}$$

with the mass m of the subhalo, the density of the background ρ, the velocity v of the subhalo, the Coulomb logarithm $\ln\lambda$ and the velocity dispersion of the medium σ[5]. As a consequence, the orbit contracts, the pericenter becomes smaller, and the orbit gradually tightens. According to Equation (2.13), the tidal radius therefore also becomes smaller, leading to increased tidal stripping. When the subhalo has reached the center, it can either undergo tidal disruption or merging (*Step 3*). The time until merging or tidal disruption can be estimated with the dynamical friction timescale [78]

$$t_{fric} = \frac{1.17}{ln\Lambda} \cdot \frac{r_{circ}^2 V_{vir}}{G m_{sub}} \tag{2.15}$$

with the time until spiral-infall (merger) t_{fric}, the Coulomb logarithm $\ln\Lambda$, the radius of a circular orbit with the same energy r_{circ} and the virial velocity of the host halo

$$V_{\mathrm{vir}} = \sqrt{\frac{GM_{\mathrm{vir}}}{R_{\mathrm{vir}}}} \tag{2.16}$$

If the subhalo *merges*, it becomes incorporated in the main halo (see Fig. 2.3). In case of tidal disruption, tidal forces near the apocenter disrupt the subhalo, causing a leading and trailing tail. This can lead to the creation of a stellar stream [119] (see Subsubsec. ▶ 2.3.1.1).

[4]This can potentially give rise to a stellar stream. GD-1, on the other hand, is believed to have originated from a GC, which does not possess a DM subhalo.

[5]This effect particularly plays a role for massive subhalos (approximately $m > 10^9 M_\odot$).

2.1.2.3 The Small-Scale Crisis

While the ΛCDM model provides an excellent description of the universe on cosmological scales[6], there are some discrepancies between simulations and observations on galactic and sub-galactic scales. These discrepancies are the motivation behind the development of modifications to the CDM model, such as SIDM and *Dissipative Self-Interacting Dark Matter* (DSIDM) (for a description of the specific models see Subsec. ▶ 2.2.2). In the following, these issues, also referred to as the *small-scale crisis*, are briefly discussed, as well as, how SIDM and DSIDM can contribute to its solution [127, 28, 32]:

- *The core-cusp problem*: CDM simulations have shown that the mass density profile increases for $r \to 0$ and predict a *cuspy* density profile [50, 93, 94]. However, observations of the rotation curves of disk galaxies favour *cored* density profiles $\alpha \sim 0$ at small radii [89, 88]. This problem is adressed by the the SIDM modell, as Figure (2.4) shows by comparing simulations of a galaxy density profile with two standard profiles for CDM and SIDM. In this model, self-interactions between the DM particles alter the density profile towards a core in the center (see Subsubsec. ▶ 2.2.2.2).

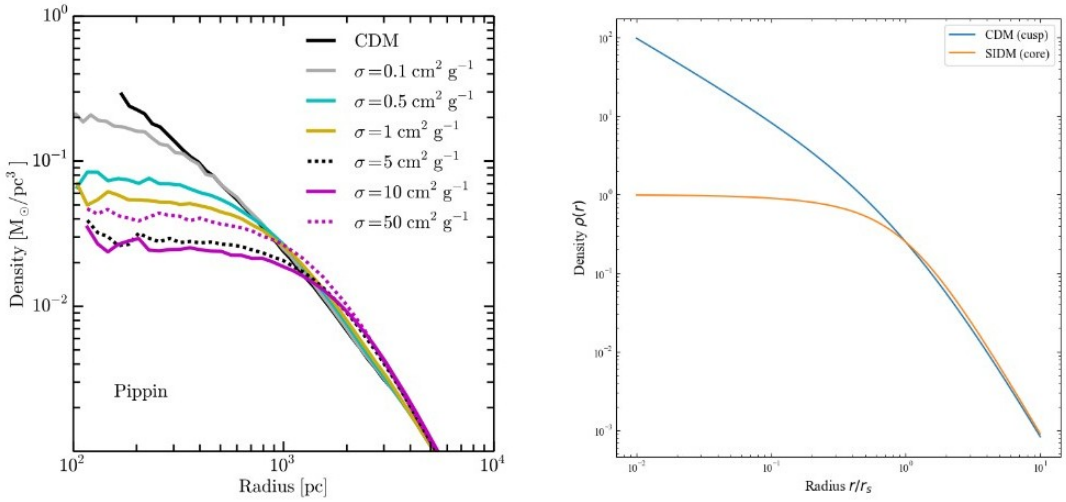

FIGURE 2.4: N-body simulations of different density profiles (from [54], left) and two typical density profiles (cuspy *Navarro-Frenk-White* (NFW) [94]) and cored Einasto [53]) for comparison. The SIDM model used in this work is based on a cross section of $\frac{\sigma}{m} = 5\,\mathrm{cm}^2\,\mathrm{g}^{-1}$.

- *The diversity problem*: Simulations in the ΛCDM model predict that galaxies of similar mass should have similar rotation curves, as DM halos follow a universal

[6] *Cosmological scales*, contrary to *galactic scales*, describe the big structure of the universe, ranging from galaxy clusters to the whole universe.

profile (e.g., NFW). Observations, however, show a wide range of inner rotation curve shapes [96]. Some galaxies have steeply rising curves (= cuspy halos), while others rise more slowly (= cored halos)[7]. By implementing, in addition to the self-interactions in the SIDM model, also dissipative effects, DSIDM can produce super-cuspy profiles. Through the combination of these two mechanisms, the diversity problem can be addressed.

- *The missing satellites problem*: When looking at the structure of a galaxy, according to the standard model, each galaxy is assigned exactly one DM halo. The equivalent for a dwarf galaxy, also referred to as a satellite, would be a subhalo (although not every subhalo necessarily contains a DG). However, based on the number of subhalos in a galaxy, one can also expect a certain number of satellites. As CDM halos form through the merging of smaller halos, they are expected to contain a significant number of subhalos [73]. This is due to the hierarchical formation process, explicated in the section above, where structure grows from the bottom up, with small halos collapsing first and later merging into larger systems. Therefore, remnants of these early halos should persist as subhalos within the newly formed larger DM halos. However, the observed number of small galaxies in the Local Group is significantly lower than the predicted number of subhalos. For example, in the MW, only about 10 dwarf spheroidal galaxies have been discovered, whereas simulations predict on the order of 100–1000 subhalos [90, 74]. SIDM addresses the Missing Satellites Problem by altering the internal structures of subhalos through self-interacting dark matter, reducing their survival probability within the main halo, which leads to fewer visible satellites [132]. DSIDM extends this model by including dissipative effects that can cause additional energy losses in small subhalos, resulting in even stronger mass reduction and a changed number of satellites [60]. However, neither of the two models can fully explain the problem, so further (astrophysical) solutions need to be found.

- *The Too-Big-To-Fail Problem*: CDM simulations initially predicted that the brightest satellites of the Milky Way would correspond to the most massive subhalos, as these are expected to have the highest chances of hosting observable galaxies. However, studies have shown that subhalos in the central regions of the MW are much denser than expected [28]. These subhalos are so massive and dense that they should have been capable of forming stars, meaning they should host visible satellite galaxies. However this galaxies are not observed, creating a discrepancy. SIDM addresses this problem by creating cored density profiles in massive subhalos, reducing their central densities, so they no longer appear *too big to fail*.

[7] For the rotation curve of the MW, see [40].

2.2 Dark Matter

2.2.1 General Concepts

2.2.1.1 Problems with the Standard Model

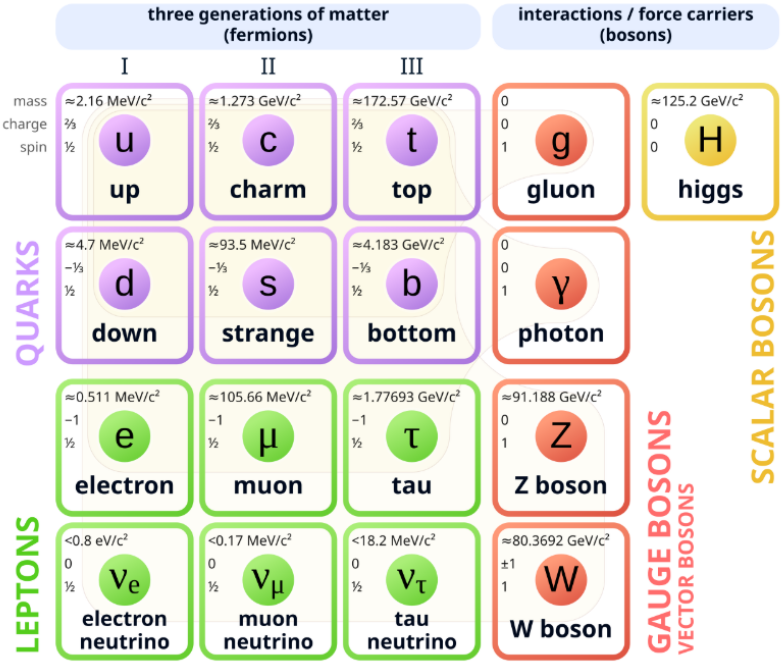

FIGURE 2.5: The components of the Standard Model of particle physics are fermions (= building blocks of matter) and bosons (= mediators of the fundamental interactions). The fermions are organized into three generations in order of increasing mass, with the first generation constituting the stable matter that makes up our everyday world. The four gauge bosons mediate the fundamental forces (photon: electromagnetic, gluons: strong, W/Z bosons: weak), whereas the Higgs boson is responsible for generating mass [42].

In physics, four fundamental interactions are known. Three of them are described by the *Standard Model of particle physics*: the *electromagnetic force* (described by quantum electrodynamics, QED [48]), the *weak interaction* (described by the electroweak theory), and the *strong interaction* (described by quantum chromodynamics, QCD [62]). The model distinguishes between matter particles (= fermions) and force-carrying particles (= bosons), which mediate the interactions between them, as Figure (2.5) illustrates[8]. Through various mechanisms (e.g., thermal radiation, radioactive decay, electron transitions), matter produces electromagnetic radiation that can be observed with telescopes,

[8]The standard model has been experimentally confirmed step by step troughout the 20th and 21st century, most recently through the discovery of the Higgs boson at CERN in 2012 [1].

because photons can be described as waves due to the wave-particle duality. This radiation spans the entire electromagnetic spectrum, of which only a small portion corresponds to the wavelength range detectable by the human eye. The three interactions described by the Standard Model of Particle Physics can be probed either directly (as in the case of the electromagnetic interaction via light) or indirectly (such as the weak and strong interactions through neutrino or cosmic ray signals). The fourth fundamental force of physics, *gravity* [86], however, cannot be observed with telescopes. Nevertheless, there are ways to determine gravity, such as motion of celestial bodies, gravitational lensing, tidal forces, or gravitational waves. In principle, the amount of matter detected with telescopes should thus be confirmable through these measurements. In fact however, several discrepancies have emerged. Particularly five of them have been central [14]:

- *Rotation velocity of clusters*: Even if the existence of an unseen matter in the MW was taken into consideration earlier, Fritz Zwicky was the first scientist explicitly introducing the term *Dark Matter* [136]. The velocity of galaxies orbiting a cluster is given by

$$v \approx \sqrt{\frac{GM}{R}} \tag{2.17}$$

  with the total mass of the cluster M, the radius of the cluster R and the gravitational constant G. He observed that galaxies within the *Coma Cluster* were moving at velocities too high to be held together by the visible mass alone. Applying the virial theorem, he deduced that there must be a significant amount of unseen mass providing the necessary gravitational pull[9] [136, 137].

- *Rotation velocities of galaxies*: In 1970, Vera Rubin investigated the rotational velocities of stars in spiral galaxies and discovered the same phenomenon on a galactic scale. According to the relation $v \propto 1/\sqrt{r}$, following Equation (2.17), stars farther from the center should rotate more slowly. However, observations showed that they rotate at nearly constant speeds [109, 108]. Figure (2.6) shows this on the example of the spiral galaxy M33.

- *Gravitational lensing*: This occurs when massive objects, like galaxy clusters, bend the light from background sources. Observations revealed that the amount of lensing could not be accounted for by visible matter alone [128, 38, 85, 30].

[9] This does not necessarily mean that DM interacts only gravitationally. For example, there are models that assume a coupling to Standard Model particles (see Subsubsec. ▶ 2.2.1.2). The essential property of DM, however, is that it does not interact with the electromagnetic spectrum and is therefore invisible to direct observation.

- *The Cosmic Microwave Background*: Measurements of the *temperature fluctuations* of the CMB revealed that the density of visible matter cannot explain the peaks in the power spectrum [117, 3].
- *Structure formation and large-scale distribution*: The distribution of galaxies and galaxy clusters across the universe reveals a web-like structure that developed from tiny primordial density fluctuations, visible in the CMB and serving as initial conditions for the structure formation (see Subsubsec. ▶ 2.1.2.1). Models with only baryonic matter fail to reproduce the correct timing and scale of these structures. Therefore, structure formation strongly supports the existence of DM [14, 122].

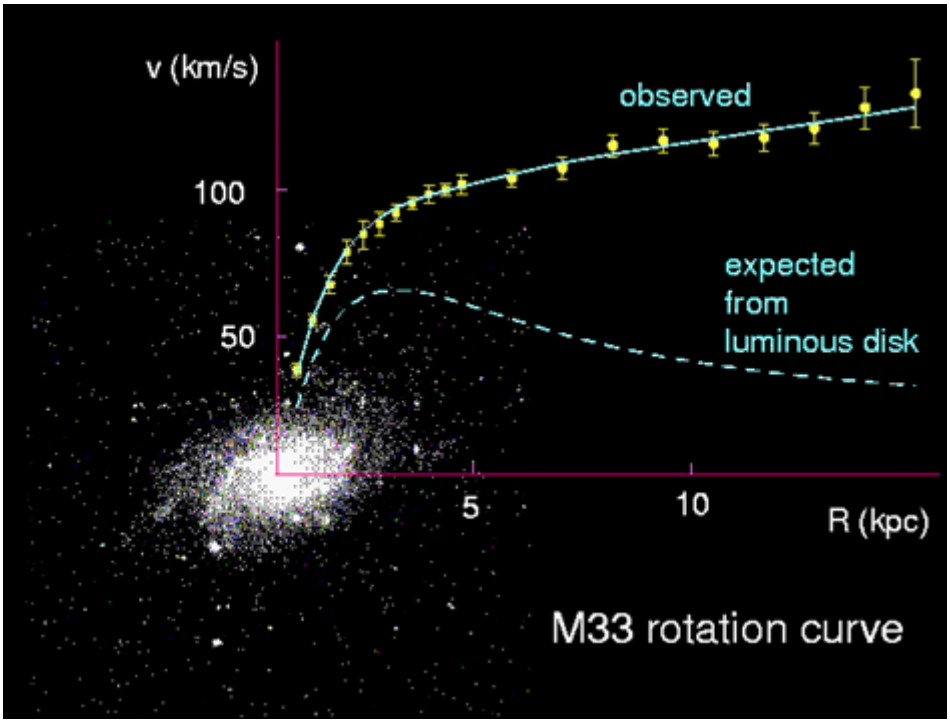

FIGURE 2.6: Rotation curve of the spiral galaxy M33 [41, 110].

2.2.1.2 Dark Matter Particle Models

Since the second half of the 20th century, a wide variety of theories, models, and particle candidates have been developed to explain the discrepancies. Figure (2.7) shows a possible way to structure the various particle models [63][10]. The process of *structure formation* (see Subsubsec. ▶ 2.1.2.1) depends on the velocity of the DM particles during the time when the structures are forming. Faster-moving particles (such as *Warm Dark*

[10] Alternative approaches are the so-called Modified Gravity and the idea that DM could consist of compact objects. While the former is still actively debated, the latter is currently considered as less probable [36, 59].

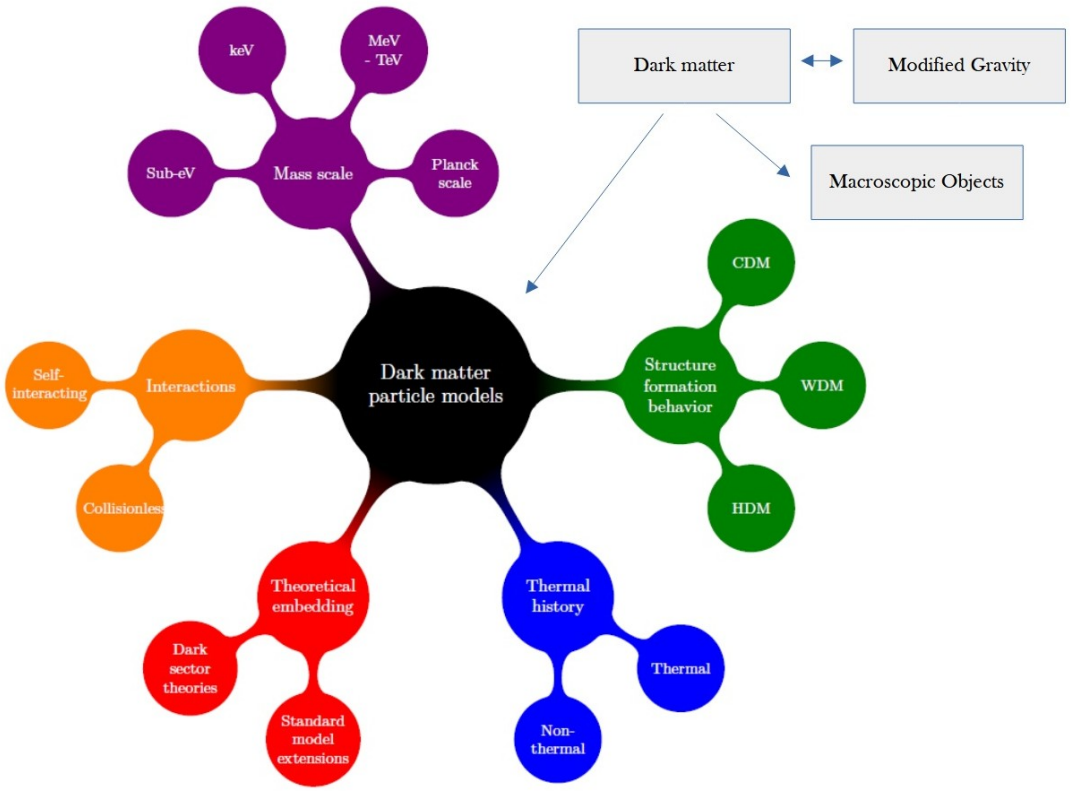

FIGURE 2.7: Possible classification scheme of DM particle models (colored region). These can, for example, be distinguished by their kinetic energy or *structure formation behavior*, their *(non-)thermal history*, their *mass*, and possible *self-interactions*. They may either be embedded within the Standard Model or described within a separate so-called *dark sector* (such as SIDM and DSIDM).

Matter (WDM) or *Hot Dark Matter* (HDM)) erase smaller density fluctuations more quickly, so that in this case, instead of the hierarchical structure formation described in the previous chapter, large structures form first [23][11]. DM could have formed thermally or non-thermally (see Subsubsec. ▶ 2.1.2.1). SIDM and DSIDM are both so-called *Dark Sector* models [67]. This means, they involve their own interactions that cannot be classified under the known interactions of the Standard Model. Furthermore, DM models can include *self-interactions* or not, whose strength are typically characterized by the interaction cross section per unit mass, usually in the range $\sigma/m \approx 0.1 - 10\,\mathrm{cm}^2/\mathrm{g}$. Larger values are considered strong, smaller values weak [127]. The mass of possible candidates spans a wide range from ultralight ($\approx 10^{-22}\,\mathrm{eV}$) to the Planck scale.

[11] However this does not match the observations [44].

2.2.2 Specific Models

2.2.2.1 Cold Collisionless Dark Matter

CDM is the most common model for DM and a part of the so-called ΛCDM model [8], the standard model of cosmology [72]. During tiny density fluctuations formed due to quantum fluctuations, the slow velocity of CDM particles (therefore the term *cold*) allowed gravitational aggregation in regions with a high density of matter. This process allowed for the growth of small structures that could merge into larger ones, a phenomenon known as *hierarchical structure formation*, described above (see Subsec. ▶ 2.1.2). It explains the observed large-scale structure of the universe, with galaxies and clusters arranged in a filamentary pattern[12]. CDM particles do not interact with each other, so no heat conduction occurs. As a result, DM structures such as halos can remain stable over long timescales.

2.2.2.2 Self-Interacting Dark Matter

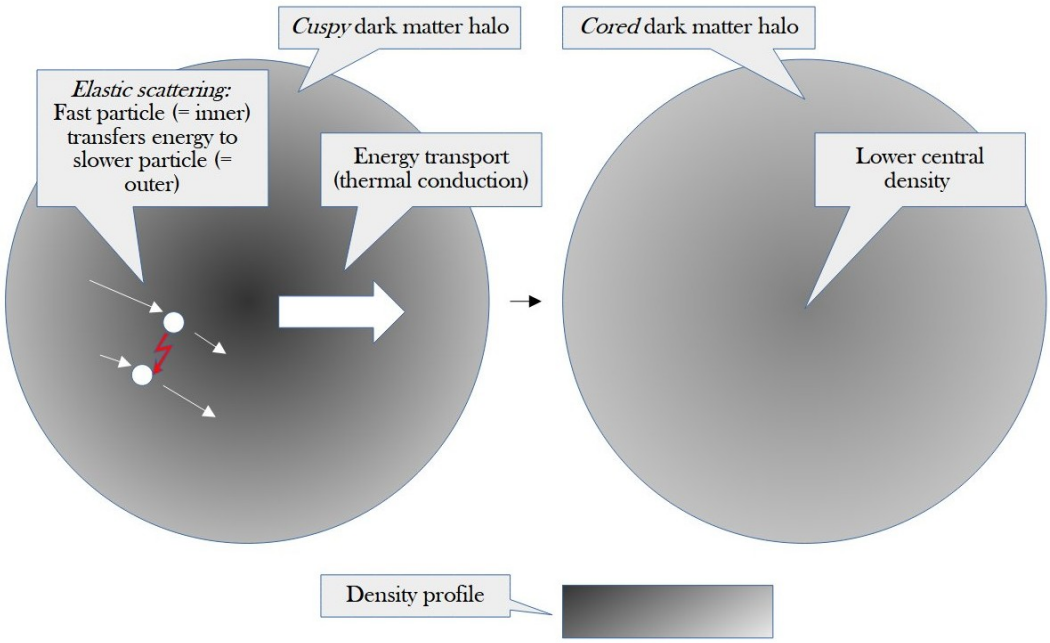

FIGURE 2.8: This figure provides an illustrative representation of energy transport via thermal conduction in SIDM. As a result, energy flows from the hot central region outward, leading to a flattening of the central density profile.

[12]In contrast, WDM, and even more so HDM, would result in a smoother structure, inconsistent with observations, because the higher speed of WDM particles prevents them from accumulating strongly in the potential wells [22].

SIDM was introduced as a possible solution to the small-scale crisis, notably the core–cusp problem. The original model proposed by Spergel and Steinhardt [118] was based on *elastic scattering*. The self-interactions are thus modeled as $2 \to 2$ scattering processes. Figure (2.8) illustrates, how the core-cusp-problem can be adressed with this model. Particles located closer to the center of the halo are more strongly attracted by the overall gravitational potential of the halo and therefore require a higher velocity to remain in place. Otherwise, they could fall inward, leading to gravitational collapse[13]. When two SIDM particles scatter elastically, a faster-moving particle from the inner region may collide with a slower one from farther out. As a result, energy is transferred from the inner to the outer region [104, 75, 54]. The slower particle gains energy and moves outward, while the faster one loses energy and sinks inward or remains. Statistically, this leads to a net outward flow of energy (= heat conduction). The particles in the center thus lose energy, move more slowly and the pressure decreases. As a result, the density profile in the center becomes flatter (*core* instead of *cusp*). The precise implementation of self-interactions depends on the specific SIDM models, that can be classified into *velocity-independent* and *velocity-dependent* scenarios. In velocity-independent SIDM, particles scatter with a fixed probability regardless of their relative velocity, which leads to uniform heat conduction in halos of all sizes. In velocity-dependent SIDM, the scattering probability depends on the relative velocity. In this work, a velocity-independent model is used (which means, the cross section per unit mass σ/m is fixed). To describe the subhalo profile, the solution of the gravothermal fluid equations for a spherically symmetric gas is employed, where self-interactions are modeled via *heat conduction*. To describe this, one can start with [114]

$$q = \frac{L(r)}{4\pi r^2} \tag{2.18}$$

Here q is the radial heat flux and L the luminosity. According to Fourier's law of *heat conduction*, the heat flux in a medium is proportional to the temperature gradient. The one-dimensional expression in a spherical symmetry is

$$q(r) = -\kappa \frac{\partial T}{\partial r} \tag{2.19}$$

κ is the thermal conductivity, which describes the heat conduction ability of a medium. From this, the following expression can be derived:

$$\frac{L}{4\pi r^2} = -\kappa \frac{\partial T}{\partial r} \tag{2.20}$$

[13] Which is typically the case for $\sigma/m > 10\,\mathrm{cm}^2/\mathrm{g}$ [55]. This reflects the concept of the virial theorem: in a stable halo, gravitational forces and kinetic energy are balanced.

As shown in Figure (2.8), the scattering processes in SIDM lead to a heat flux similar to that in a gas. This situation can be described by the so-called *gravothermal fluid equations* [114]

$$\frac{\partial M}{\partial r} = 4\pi r^2 \rho \tag{2.21}$$

$$\frac{\partial(\rho\nu^2)}{\partial r} = -\frac{MG\rho}{r^2} \tag{2.22}$$

$$\frac{\partial L}{\partial r} = -4\pi\rho r^2 \nu^2 \left(\frac{\partial}{\partial t}\right)_M ln\frac{\nu^3}{\rho} \tag{2.23}$$

$$q(r) = -\kappa\frac{\partial T}{\partial r} \tag{2.24}$$

These equations are also able to describe the heat conduction toward the center, which in turn results in a flatter density profile. The SIDM density profile used in this work is based on a numerical solution of them. While the gravothermal fluid equations describe the time evolution of the *halo as a whole*, the *local relationships* between the state variables of the SIDM fluid are described thermodynamically (for the derivation, see ▶ A.2) [24]

$$\frac{\partial L}{\partial r} = -4\pi\rho r^2 \nu^2 \left(\frac{\partial}{\partial t}\right)_M ln\frac{\nu^3}{\rho} \tag{2.25}$$

2.2.2.3 Dissipative Self-Interacting Dark Matter

Inelastic scattering on the other hand refers to collisions where DM particles change their internal states or convert into different particles, resulting in a transfer or loss of kinetic energy. Unlike elastic scattering, which conserves both kinetic energy and particle identity, inelastic processes can be exothermic or endothermic, causing energy to be released or absorbed during collisions [127]. In the exothermic case, where energy is released (e.g. through the emission of radiation) the interaction can be described as DSIDM, provided that the energy loss leads to a net dissipation from the system. In DSIDM, DM particles not only interact with each other via self-scattering (as in SIDM) but also have the ability to dissipate energy, typically through weak interactions or other mechanisms that allow for the loss of kinetic energy. This dissipation leads to the cooling of dark matter, causing it to cluster more efficiently in the central regions of halos, which can help address the core-cusp problem by softening the central density profile, resulting in a cored structure rather than a steep cusp. In comparison to traditional SIDM, which involves elastic scatterings that redistribute energy, but do not result in cooling, DSIDM adds dissipative processes, that cause DM particles to lose energy over time. This can lead to a more rapid concentration of DM in the centers of halos and

potentially resolve some of the small-scale structure issues that persist in the ΛCDM model. In the thermodynamic description (see Eq. 2.25), a cooling term (in form of the cooling rate C) needs to be included to account for the energy loss due to the inelastic scattering [114]

$$\frac{\partial L}{\partial r} = -4\pi\rho r^2\nu^2\left(\frac{\partial}{\partial t}\right)_M ln\frac{\nu^3}{\rho} - 4\pi r^2 C \tag{2.26}$$

2.3 Stellar Streams

2.3.1 General Concepts

2.3.1.1 Formation and Structure

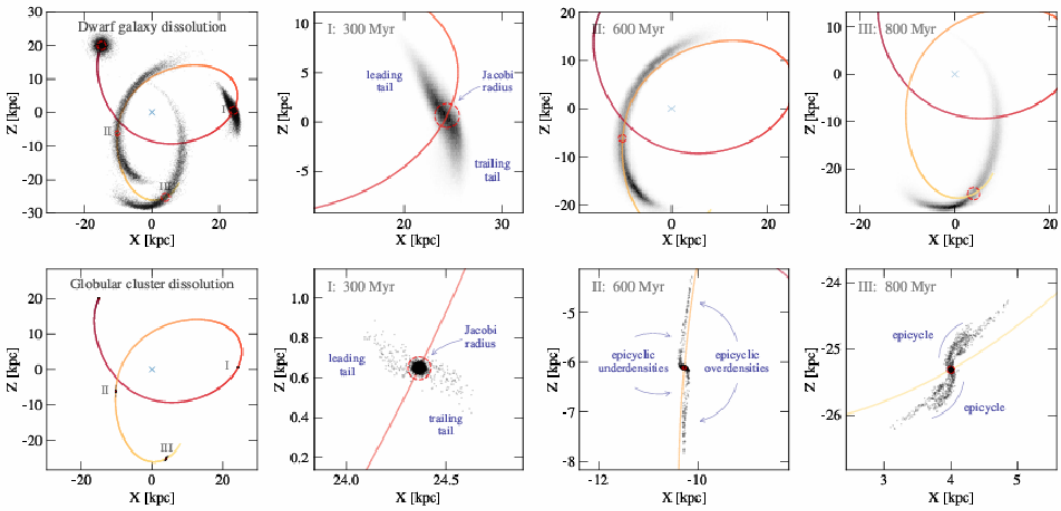

FIGURE 2.9: Numerical models of a $10^8 M_\odot$ DG and a $10^4 M_\odot$ GC, both undergoing tidal disruption along the same orbit within a MW–like gravitational potential to form stellar streams (adopted from [21]). The columns show the individual steps in the formation of stellar streams for the two cases: **Left column**: Overview of the first 10^9 years of the dissolution of the progenitor, starting at position $(X, Z) = (-15, 20)$ kpc. The Roman numerals indicate the position shown in each column. DG tails are longer than those of GC at all times. **Column I** (after 300 Myr): The progenitor already develops short leading and trailing tails, while most stars are still bound within the tidal radius (Eq. 2.13, see Subsubsec. ▶ 2.1.2.2). **Column II** (after 600 Myr): Tidal tails are longer at pericenter than at apocenter. When formed from a GC, epicyclic overdensities and underdensities become apparent, which also shape the density profile of GD-1 (see Subsubsec. ▶ 2.3.2.3). **Column III** (after 900 Myr): The tips of the tails have by now moved away from the progenitor's orbit, and the density profile of the GC streams is fully developed [21].

Stellar streams form from two possible structures, called *progenitors*, *Globular Clusters* (GC) or *Dwarf Galaxies* (DG) [130]. A fundamental difference between the two objects is, that DG are independent systems with a DM subhalo (satellites), whereas GC are only baryonic. Furthermore, DG are usually more massive ($\approx 10^6 - 10^9 M_\odot$) than GC ($\approx 10^4 - 10^6 M_\odot$) and have a larger diameter. The stellar population of GC consists almost exclusively of old stars from a single population (similar formation time and metallicity), whereas DGs contain stars from different epochs of star formation and with varying metallicities. These differences have an impact on the formation and the later structure of the stellar streams that arise from them. When considering the stages of the accretion of a DM subhalo (which simultaneously corresponds to a DG, since being surrounded by a DM subhalo is characteristic of a DG), streams predominantly form during the *tidal stripping* process (see Subsubsec. ▶ 2.1.2.2). The forming process for the two progenitors (see Fig. 2.9) differs slightly:

- *Dwarf Galaxies*: DG, due to their higher total mass, mainly from their DM halo, have a larger *tidal radius* (Eq. 2.13) and are therefore disrupted more slowly and over larger scales. The formation proceeds without a single well-defined escape point, but rather through large-scale unbinding of the outer regions. DGs usually also have a more diverse stellar population with varying age and velocity distributions. This causes streams from DGs to often be more heterogeneous and less dense.

- *Globular Clusters*: Stellar streams from GCs on the other hand, form through a relatively continuous tidal stripping. Stars escape mainly via the Lagrange points L1 and L2, located along the line connecting the cluster to the galaxy, following slightly offset orbits, causing *epicyclic motion*. An *epicycle* is a small, superimposed oscillation on top of a larger guiding orbit. The oscillation of the stars in radial direction can then be described as $r(t) = R_0 + A\cos(\kappa t + \phi)$ under the (simplified) assumption that the galactic potential is approximately axisymmetric and smooth, and that the star deviates only slightly from the guiding orbit. Here, $r(t)$ denotes the radial distance of the star from the galactic center at time t, R_0 is the radius of the guiding orbit, A the amplitude of the epicyclic motion, κ the epicyclic frequency, and ϕ the phase angle. This epicyclic motion causes stars to move faster in the inner region (pericenter, $r < R_0$) and slower in the outer region (apocenter, $r > R_0$) (see [77], for more details). As a result, the forming stream develops areas of over- and underdensities, such as those observed in GD-1 [19, 71]. Due to their highly localized escape from a compact system with low velocity dispersion, streams from GC are often thin and long with a smooth and uniform structure, making the epicyclic pattern clearly visible, which is also the case for GD-1 [115, 12, 21].

2.3.1.2 Stellar Streams in the Milky Way

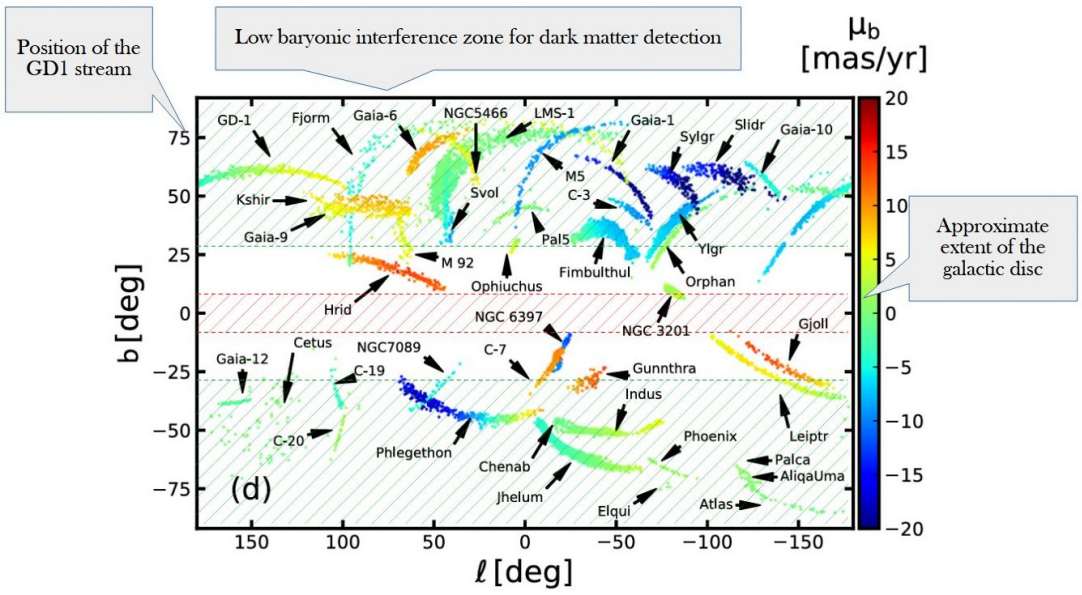

FIGURE 2.10: This figure shows a map of stellar streams in the MW in galactocentric coordinates. It covers the entire southern (b $< 0°$) and northern (b $> 0°$) hemispheres in both longitude and latitude, corresponding to the whole sky visible from earth. The *red hatching* approximately indicates the region of the galactic disk, where many interactions with baryonic matter (e.g., *Molecular Clouds* (MC)) occur, making the study of DM with stellar streams challenging. The *green-hatched* outer region marks the area where DM can be effectively investigated, provided that the streams under consideration also possess suitable properties [98, 26].

Our galaxy, the Milky Way (MW), is a *barred spiral galaxy* of type *SBbc* (S = spiral galaxy, B = presence of a central bar structure, bc = moderately wound spiral arms and an intermediate-sized bulge)[14] [70]. Its main (baryonic) components include the *bulge* (the central component, containing older mainly older stars), the *disc* (with many star formation regions) [16] and the *halo* [68]. Stellar streams in the MW have been discovered through various spectroscopic, photometric amd astrometric sky surveys. Table (2.2) lists different missions, their timeframes and major discoveries. Figure (2.10) shows a galactocentric map of the stellar streams in the MW. The galactic disk, where most of the baryonic matter is concentrated, lies around galactic latitude 0, typically within a range of approximately $b = -10°$ to $b = 10°$ (thick disc). Stellar streams that are well suited for analyzing potential dark matter interactions are typically found in regions far from the galactic disk (at higher galactic latitudes, $|b| > 20° - 30°$). In these regions, the contamination from gas, dust, star fields, and other baryonic structures is much less

[14] In some classifications, it is also broadly referred to as type *Sc* or *Sbc*, due to its loosely wound spiral arms and relatively small bulge [129, 111].

strong. To study DM through its interaction with a stellar stream, it is also advantageous if the stream possesses the following properties:

- *Dynamically cold nature*: Intrinsically dynamically cold streams exhibit a lower internal velocity dispersion (also referred to as intrinsic noise, $\sigma \leq (2-3)\,\mathrm{km/s}$). This makes perturbations more visible [83, 20, 33, 2, 35].
- *Large angular length and well-determined stellar membership*: Streams with substantial angular length and precisely identified member stars enable a clearer baseline for detecting structural irregularities [99].

Source	*Era*	*Stream discoveries*
Sloan Digital Sky Survey (SDSS)	2001-2010	Palomar5 (2001), GD-1 (2006) Orphan (2007)
Pan-STARRS1, DES, VST, ATLAS	2010-2017	Atlas, Phoenix Tucana III
Gaia	2016-today	>60 streams, Jhelum, Gaia-Enceladus debris, Helmi

TABLE 2.2: Sky surveys that lead to the discovery of stellar streams in the MW. While SDSS [57], Pan-STARRS1 [13], and DES Tucana [49] were both photometric and spectroscopic missions, Gaia [39] enabled highly precise measurements of stellar proper motions in the streams thanks to its astrometric data.

2.3.2 The GD-1 Stream

2.3.2.1 Properties

The GD-1 stream was first discovered in 2006 by Grillmair and Dionatos in photometric data from the Sloan Digital Sky Survey (SDSS) [65]. With the advent of Gaia data, especially Data Release 2 (DR2) and DR3, its spatial extent, distance profile, and full 6D phase-space structure have been significantly refined [84, 105]. GD-1 has a physical length of approximately 14 kpc [83] and a width of about $20-30\,\mathrm{pc}$ [105]. The stream lies at heliocentric distances ranging from roughly $8-13\,\mathrm{kpc}$, with a mean distance around 10 kpc [46]. Its galactocentric radius varies accordingly, averaging around 13 kpc, and its vertical position relative to the Galactic plane is about 10 kpc, placing it well within the stellar halo [46]. GD-1 is on a retrograde, eccentric orbit around the MW, with an estimated eccentricity of $e \approx 0.3-0.4$ and an orbital period of roughly $500 \cdot 10^6\,\mathrm{yr}$ [83]. The stream passes between a pericenter of $\approx 13\,\mathrm{kpc}$ and an apocenter near $20-25\,\mathrm{kpc}$ [76]. Radial velocities along the stream vary from approximately $-100\,\mathrm{km/s}$ to $+50\,\mathrm{km/s}$, depending on the position along the stream [105].

2.3.2.2 Origin

Despite extensive searches, no clearly bound remnant of the progenitor cluster has been conclusively identified. There are tentative overdensities along the stream (for example near $\phi_1 \approx -13°$) [105], but none shows the properties expected of a surviving core. Nevertheless, the progenitor is believed to have been a GC for several reasons. First, the narrow width of only about 20 pc [105] is characteristic for streams originating from relatively compact, massive and dense systems like GCs, whereas DGs are larger and more diffuse, producing wider and less dense streams [55]. The compactness of a GC results in small velocity differences among the tidally stripped stars, which leads to a narrow and coherent stream[15]. Another strong argument is the low velocity dispersion of typically less than 1 km/s [76, 83], which reflects the much higher compactness of a GC. In contrast, DG usually exhibit higher internal velocity dispersions (typically around $5 - 10$ km/s), which would result in wider streams with greater kinematic spread. The total energy of escaping stars is defined as

$$E_{\text{star}} = \frac{1}{2} v_{\text{rel}}^2 + \Phi_{\text{GC}}(r) > \Phi_{\text{MW}}(r) \tag{2.27}$$

where v_{rel} is the velocity of the star relative to the cluster and $\Phi_{GC}(r) \sim \frac{GM}{r}$ the gravitational potential of the progenitor. Stars escape when their total energy exceeds the MW's potential at that location, $E_{star} > \Phi_{MW}(r)$. A higher internal velocity dispersion in DGs leads to larger values of v_{rel}^2, and thus to broader, dynamically hotter streams. The metallicity[16] has been identified as [Fe/H] $\approx$ 2.0 to 2.1 [83]. Such a low metallicity is typical for a GC, which typically hosts old and metal-poor stars. Furthermore, the kinematic sharpness and orbital coherence of GD-1 argue against the presence of a DM halo, supporting a purely baryonic origin. Above this, in streams formed from DGs, one often finds a surviving core remnant due to their larger mass. However this is not observed in GD-1.

2.3.2.3 Density Profile and Perturbation

Figure (2.11) shows the density profile along the GD-1 stream. Papers that have investigated its density structure (see [19], for example) have identified several notable characteristics. The presence of so-called epicyclic overdensities in a stellar stream is a common phenomenon, resulting from the process of tidal stripping from the progenitor

[15] The width σ_x of a cold stream can be approximated by $\sigma_x \approx \sigma_v \cdot t$, where σ_v is the velocity dispersion of the progenitor and the time since the stars were stripped.

[16] Metallicity is defined as the ratio of iron to hydrogen compared to the Sun, given by $[\text{Fe/H}] = \log_{10}\left(\frac{N_{\text{Fe}}}{N_{\text{H}}}\right)_{\text{object}} - \log_{10}\left(\frac{N_{\text{Fe}}}{N_{\text{H}}}\right)_{\odot}$.

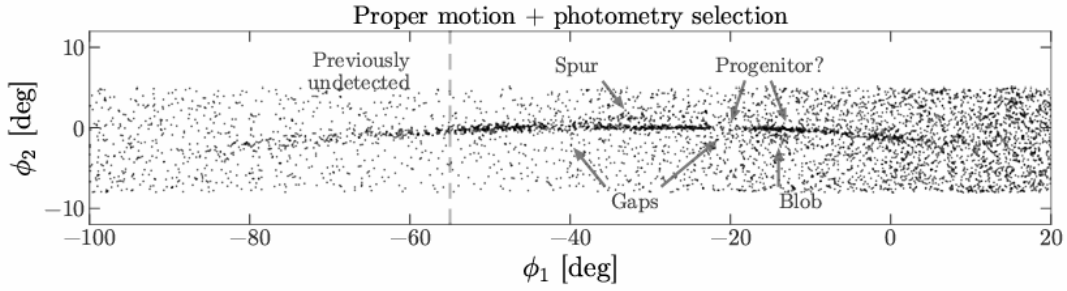

FIGURE 2.11: The density profile of GD-1 shows the two gaps at $\phi_1 = -40°$ and $-20°$, as well as the *spur* next to the gap at $\phi_1 = -40°$. This is one of the reasons why a collision with a compact object is assumed to be the cause, rather than an epicyclic underdensity [19].

(see Subsubsec. ▶ 2.1.2.2 and ▶ 2.3.1.1)[17]. Two prominent density gaps at $\phi_1 = -20°$ and $\phi_1 = -40°$ stand out and could originate from different physical processes [19]. The gap at $\phi_1 = -20°$ coincides precisely with the location of the presumed progenitor of GD-1 [19]. According to models of epicyclic stellar release, such a gap is expected at this position, since no new stars are being stripped there anymore. Just before and after the gap, epicyclic overdensities are observed, as the last stars released from the progenitor accumulate in these regions. The gap at $\phi_1 = -20°$ is therefore considered a natural consequence of the stream's formation. In contrast, the gap at $\phi_1 = -40°$, in the interpretation of [19] is attributed to a perturbation by a massive external object. This argumentation is supported first by the gap's morphology: it is relatively broad (several degrees wide) and asymmetric, whereas epicyclic gaps are typically narrow and regular. Secondly, a lateral overdensity (the so called *spur*) is visible in the range $\phi_1 \approx -40°$ to $-30°$, located above the main stream (= vertically offset in ϕ_2). This spur is not compatible with the expected stream path and could be explained by a gravitational kick from an external perturber. Simulations show that such a feature can only result from a close encounter with a massive object, with an estimated mass of about 10^6 to 10^7 $M_\odot$. It should be emphasized, that there are also opinions considering the spur as a normal part of the epicyclic stream-fanning pattern, citing the regularity observed in the density power spectrum as justification [71] (see also the discussion in Sec. ▶ 4.2). If the gap is caused by an external perturbation, a DM subhalo could be an object that might realistically be able to explain it. Larger subhalos usually host a DG that should be visible. However, if a DM subhalo has a lower mass then $3 \times 10^8 M_\odot$, gas is unable to cool enough to enable star formation, such that subhalos with lower mass remain

[17] A compact star cluster is gradually disrupted by the galactic gravitational field, primarily at the Lagrange points in the leading and trailing directions. Due to differential rotation within the galaxy's potential, a released star's orbit becomes superimposed with an epicyclic motion. Because stars are released with slightly different velocities, this leads to phase mixing, causing them to accumulate at specific locations along the stream. These regions appear as epicyclic overdensities.

non-baryonic [34]. Beside this, Bonaca et al. [19] considered several known objects as potential candidates for a past encounter with GD-1. Figure (2.12) shows the distance of various known baryonic objects that could plausibly have interacted with the stream, tracked over the past billion years. As illustrated, all of these objects have remained at least 1 kpc away from GD-1 during that time. Figure (2.13) displays the mass and size a perturbing object would need in order to produce the gap observed at $\phi_1 = -40°$. Overlaid are the properties of known GCs, DGs, and MCs located in the outer halo of the MW, where GD-1 resides[18]. The diagram shows, that *Molecular Clouds* (MC) are generally too diffuse and extended to qualify as plausible perturbers. Altogether, this evidence suggests that an encounter with a known baryonic object is unlikely. However, ruling out such a scenario with certainty would require precise knowledge of the underlying gravitational potential. But the orbits of both GD-1 and any potential perturber could have been significantly influenced by the gravitational effects of two massive MW satellites: the Large Magellanic Cloud and the Sagittarius DG. Due to the shape of the gap (broad and asymmetric), the presence of a vertically offset spur, and the fact that no known baryonic perturber has been identified to date, such a scenario appears highly unlikely. Based on current knowledge, the most plausible explanation is therefore a perturbation by a DM subhalo.

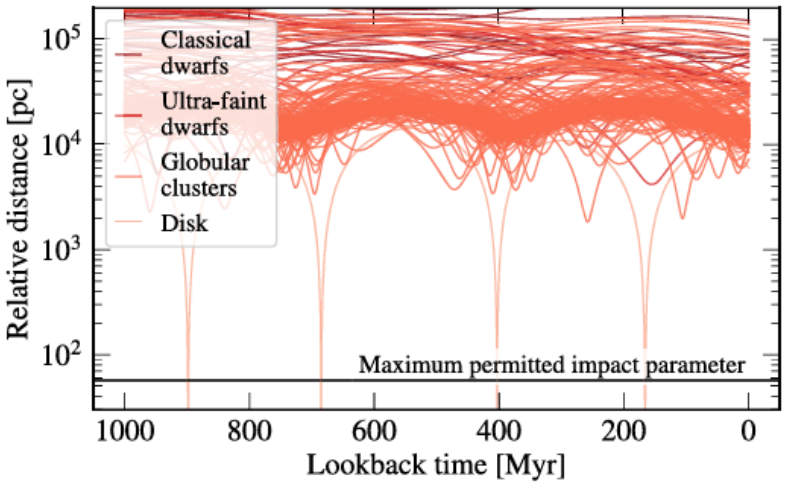

FIGURE 2.12: This figure shows the distance between the gap in GD-1 and known dwarf galaxies (dark red), ultra-faint dwarf galaxies (red), globular clusters (orange), and the stellar disk (light orange). Also shown is the *maximum permitted impact parameter* (the largest distance at which an object could pass by and still produce an observable disturbance). From the figure, it is visible that no known object has come close enough to GD-1 (from [19]).

[18]This comparison is primarily conceptual, as the different classes of objects are characterized by different density profiles.

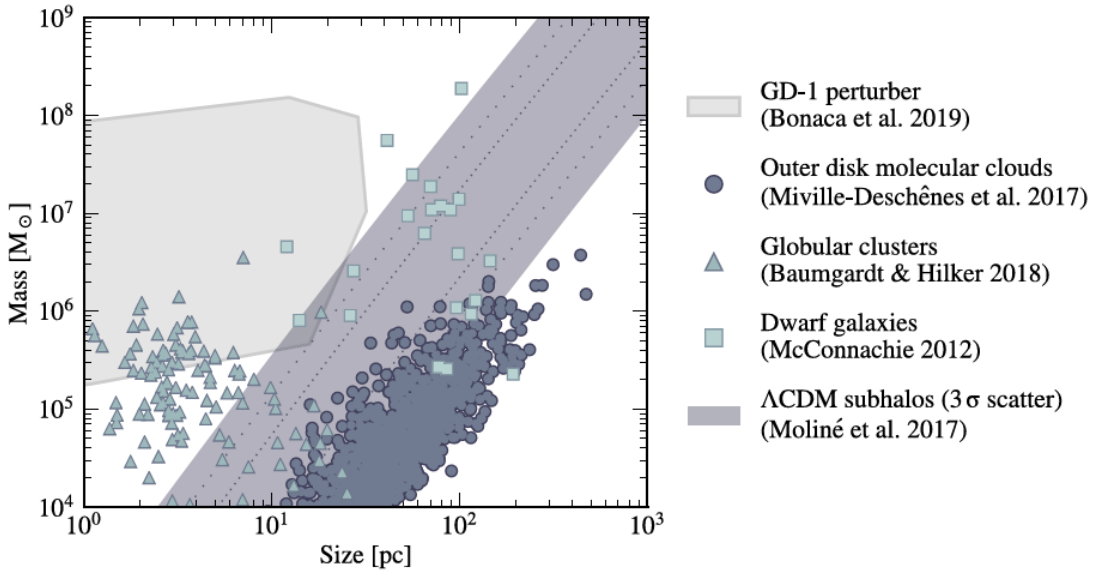

FIGURE 2.13: This figure shows the inferred mass and scale radius of the GD-1 perturber compared to known DGs (squares), GCs (triangles), and MCs (circles) in the outer disk. From this, it can be concluded that molecular clouds are not compact enough to have caused the gap at $\phi_1 = 40°$ in GD-1, while known GCs and DGs are excluded due to their orbital properties (from [19]).

2.4 Spectral Analysis

2.4.1 General Concepts

2.4.1.1 Fourier Transform and Power

A power spectrum shows how the energy of a signal is distributed across its frequency components. It indicates which frequencies are dominant and how strongly they are represented. It can be distinguished between the *Power Spectrum* (unit: power) and the *Power Spectral Density* (PSD) (unit: power per Hz). While the former expresses how much power is contained in a frequency component, the PSD describes the density of the power distribution by normalizing the power with respect to the width of the frequency bins [123]. In this work, a power spectrum is determined. Figure (2.14) illustrates this concept using two contrasting examples. To achieve this goal, the so-called technique of *Fourier transform* is used. This technique decomposes a signal into a sum (or integral) of sine and cosine functions, that is, into harmonic oscillations of different frequencies [29]. This decomposition is based on the idea that a function in most cases can be represented as a superposition of basis functions, which are, in case of Fourier analysis, the complex exponential functions. The Fourier transform $\tilde{\rho}(k)$ of a discrete signal, called *Discrete*

Fourier Transform (DFT), is defined as

$$\tilde{\rho}(k) = \sum_{n}^{N-1} \rho_n e^{-2\pi i \frac{kn}{N}}, \quad k = 0, 1, ..., N-1 \tag{2.28}$$

with the discrete signal ρ_n, the total number of sampling points N, the spatial or temporal index of the original signal n (depending on whether one considers positions or time steps) and the index k of the frequency components. If this would directly be applied in this work, ρ_n would correspond to the *counts in each individual bin*, N would be the *total number of bins* along the stream, n would represent the *index of the individual bins* with $n \in \{0, \ldots, N-1\}$, and $k \in \{0, \ldots, N-1\}$ would denote the respective *frequency components*[19]. The power $P(k)$ can then be calculated with

$$P(k) = |\tilde{\rho}(k)|^2 \tag{2.29}$$

2.4.1.2 Welch Method

In principle, it is possible to apply the Fourier transform directly, a method commonly referred to as *periodogram* [112]. However, this leads to a couple of problems, of which two are particularly noteworthy. *Variance* describes how much the result of a power spectrum estimate can vary when using different parts of the data. When using a periodogram, the result can be very noisy, because it strongly depends on the specific data segment. This makes it hard to see the real underlying frequency structure. *Spectral leakage* happens when a signal is cut off at the edges because only a finite time window is used. This can cause energy from one frequency to spread into neighboring frequencies in the spectrum. As a result, sharp peaks become blurred, and the spectrum can be misleading [125]. To address this problems, several methods have been developed[20]. A very common approach is the so-called *Welch method* [134], which uses two techniques: *Segmentation* means, that a signal is devided into multiple shorter overlapping segments, that can be smoothed by averaging. *Windowing* means, that a tapering function, called *window*, is applied to each segment of the segmentation before its Fourier transform to reduce discontinuities (see also Subsubsec. ▶ 3.1.2.1 for the mathematical implementation) [66].

[19] The indices n and k each consist of the same number of N discrete values, since the DFT is a linear mapping from an N-dimensional space to another N-dimensional space [97].

[20] For other methods see e.g [11, 125, 5].

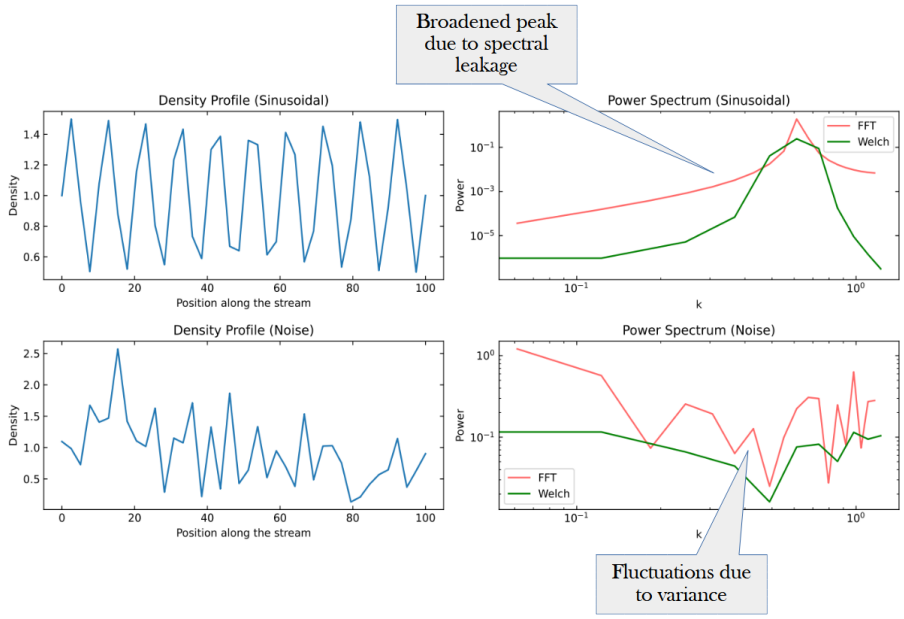

FIGURE 2.14: Illustration of two contrasting cases: A sine wave and a random signal. For both cases, the plots on the right show power spectra, once calculated with `scipy.fft` (= standard Fourier Transform) and once with `scipy.signal.welch` (= application of the Welch method [134]), each with a bin number of 40, as used throughout this work. In doing so, one can observe the effect of the Welch method on both spectral leakage and variance.

2.4.2 Density Power Spectrum of a Stellar Stream

The power spectrum determined in this work is a so-called *density power spectrum*. It describes spatial density fluctuations, or, in this case, how much the *stellar density* varies along the length of the stream. The signal in each bin is normalized by the average density in that region, determined through a fit. This density is then used as the signal input for the power spectrum calculation using a standard method (in this case: the Welch method). To obtain a more intuitively interpretable result, the frequency can be plotted inversely (as $1/f$) on the x-axis and the square root of the power on the y-axis. This way, the unit on the y-axis corresponds to that of the input signal [Counts] and the x-axis is expressed in degrees [°]. For the result to be physically meaningful and comparable, the power needs to be normalized by the length of the considered stream segment and the sampling frequency needs to be set to 1/lengthofthebins (see Subsubsec. ▶ 3.2.2.3). The resulting spectrum shows the density fluctuations along the stream: large scales reflect broad variations, while smaller scales reveal finer fluctuations.

Chapter 3

Methodology

3.1 Physical Model

In the following section, the physical models implemented in the numerical codes are presented. This provides the theoretical background of the analysis, that was subsequently performed numerically.

3.1.1 Stream Simulation

This subsection is based on a manuscript currently in preparation [4]. It provides the theoretical foundation for the *Stream Simulation* code, which computes the positions of the stars in the GD-1 stream after a subhalo collision. These positions form the basis for determining the power spectrum. The number of subhalos involved in an impact is determined stochastically; that is, it is not fixed, but rather sampled from a probability distribution. The effect of an impact on the stream strongly depends on the density profile of the subhalo, which varies between the models, as the density profile determines, for example, the gravitational potential. The specific parameters on which the subhalo density profile depends for each model are presented in the following section.

3.1.1.1 Subhalo Profiles

For all three particle models, a classical Navarro-Frenk-White (NFW) profile forms the basis [93, 94]

$$\rho_{NFW}(r) = \frac{\rho_s}{r/r_s(1+r/r_s)^2} \tag{3.1}$$

r_s is the scale radius at which the shape of the density profile (see Fig. 2.4) changes from a shallower inner region to a steeper decline toward the outer parts. This profile is then truncated for $r > r_t$ to account for tidal stripping effects from the MW halo (as explained in Subsubsec. ▶ 2.1.2.2), according to the relation $\rho(r) = \rho_{\mathrm{NFW}}(r_t) \cdot (r_t/r)^5$. The tidal radius r_t (see Eq. (2.13), Subsubsec. ▶ 2.1.2.2) is set, for simplicity, to three

times the scale radius r_s (see also [64]). For the two dark sector models SIDM and DSIDM, several modifications are implemented:

- *SIDM*: For the case of SIDM, a time evolution over 10 Gyr is implemented by numerically solving the gravothermal fluid equations (see Eq. (2.21 - 2.24), Subsubsec. ▶ 2.1.2.1) using the Nishikawa code [9, 113]. This models show self-interactions between DM particles affect the structural evolution of the halo (see Subsubsec. ▶ 2.2.2.2). The cross section per unit mass is fixed at $\frac{\sigma}{m} = 5\,\mathrm{cm}^2\,\mathrm{g}^{-1}$. Prior to the simulation, a grid of $(M_{200}, \log(c))$ combinations is defined in order to prepare a wide range of possible subhalo models. Here, M_{200} is the mass enclosed within a radius where the mean density is 200 times the critical density of the universe [52], and $\log(c)$ is the logarithm of the concentration parameter, which describes the ratio between the halo radius and the scale radius [4].

- *DSIDM*: For the case of an additional dissipation (DSIDM), the same procedure was used. In addition, when modeling the subhalo as a gravothermal fluid, a bulk cooling rate is included to account for dissipation (see Eq. (2.26), section ▶ 2.2.2.3).

Figure 3.1 shows the associated subhalo profiles for the three models, as discussed above.

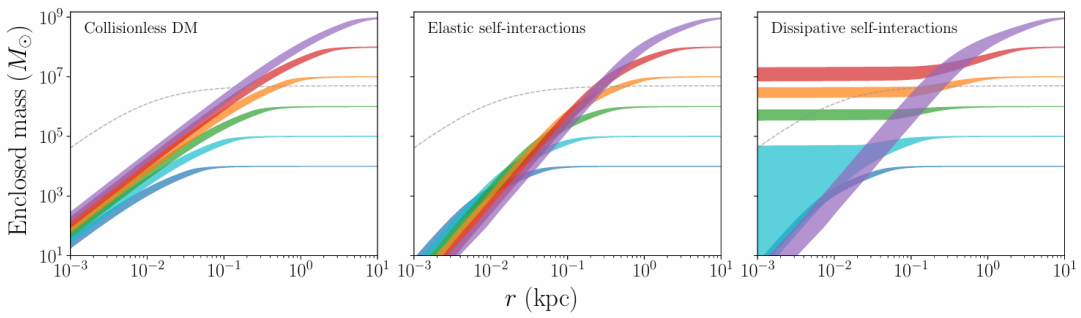

FIGURE 3.1: This figure shows the enclosed mass profiles for the three models. The greater diversity in density profiles for DSIDM is clearly visible. Also shown is the reference Hernquist subhalo profile, which was used by [19] to successfully model the spur in GD-1 [4].

3.1.1.2 Stream Simulation

For the description of the density profile, for the simulation certain models are used: A Hernquist profile for the bulge [69], a Miyamoto-Nagai disk for the disk [87] and a NFW profile for the halo. Table (3.2) shows the parameter for this constituents. The simulations are performed in galactocentric coordinates with $\vec{r}_\odot = (-8, 0, 0)\,\mathrm{kpc}$ and $\vec{v}_\odot = (12.9, 245.6, 7.78)\,\mathrm{km/s}$. As a first step, the position of every member star of GD-1

without perturbation by a subhalo encounter is determined. The galactocentric position $\vec{r}_s(t_0) = (-9.01, 6.41, 8.76)\,\mathrm{kpc}$ and velocity $\vec{v}_s(t_0) = (-160.1, -219.3, -55.4)\,\mathrm{km/s}$, corresponding the trailing end of GD-1 at the time t_0, of a tracer particle in a MW potential is time-evolved to t_i, the initial time of the simulation. Subsequently, every single star n is added to the stream by uniformly selecting stars within the time interval $t_n \in [t_i, t_i + \tau]$ with $\tau = 60\,\mathrm{Myr}$ corresponding to the time, a star needs to traverse the angular length of the stream of $\approx 100°$ on the sky. The position r_i and velocity v_i of every star is defined by

$$\vec{r}_n(t_i) = \vec{r}_s(t_n) \tag{3.2}$$

$$\vec{v}_n(t_i) = \vec{v}_s(t_n) + \delta\vec{v}_n \tag{3.3}$$

where a random shift, derived from a normal distribution of width $0.3\,\mathrm{km/s}$, is added to the velocity component, respectively. Thus, the angular width of GD-1, corresponding to $\sigma(\phi_2) \approx 0.2°$ and the dispersion in radial velocity relative to the streamline value, $\sigma(\Delta v_r) \approx 0.6\,\mathrm{km/s}$ can be replicated. As a next step, the impact of the perturbers on the stream is modeled. The trajectory of every subhalo is described as a straight line, given by the Equation [4]

$$\vec{r}_{sub}(t) = \vec{v}_{sub} \cdot (t - t_{imp}) + \vec{r}_s(t_{imp} + f_{imp}\tau) + \vec{b} \tag{3.4}$$

with the impact time t_{imp} and the impact position f_{imp}, expressed as a quantity $0 \leq f_{imp} \leq 1$ relative to the length of the stream, as well as the subhalo velocity $\vec{v}_{sub}$ [4]

$$\vec{v}_{\mathrm{sub}} = v_{\mathrm{sub}} \left(\hat{\vec{e}}_z \cos\theta - \hat{\vec{e}}_x \cos\phi \sin\theta + \hat{\vec{e}}_y \sin\phi \sin\theta \right) \tag{3.5}$$

with the orthonormal basis $\hat{\vec{e}}_{x,y,z}$. $\hat{\vec{e}}_{x,y}$ is perpendicular and $\hat{\vec{e}}_z$ parallel to the stream velocity at the position of the impact. The impact parameter $\vec{b}$ is defined as [4]

$$\vec{b} = b \left(\hat{\vec{e}}_x \sin\phi + \hat{\vec{e}}_y \cos\phi \right) \tag{3.6}$$

Table (3.1) lists the *kinematic impact parameters* which define the difference between the subhalo samples. To calculate the number of subhalo encounters, a tubular region along the stream trajectory with cylindrical radius $b_{\max}$ is considered. This region evolves over time t from $\vec{r}_s(t)$ to $\vec{r}_s(t + \tau)$. The total number of encounters $\mathcal{N}$ (= the number of subhalos that pass through this region)[1] is defined differentially as [4]

$$d\mathcal{N} = 2\pi\, v_r\, b_{\max}\, dl\, dt\, \frac{dn_{\mathrm{sub}}}{dM_{\mathrm{sub}}}\, dM_{\mathrm{sub}}\, P(\vec{v}_{\mathrm{sub}})\, d^3 v_{\mathrm{sub}} \tag{3.7}$$

[1] Only subhalos crossing through the sides are considered. The flux through the ends is neglected.

Here, l is the length along the stream, v_r the radial component of v_{sub} perpendicular to the stream, and P a Maxwell-Boltzmann distribution for subhalo velocities with width $\sigma_{sub} = 180\,\mathrm{km/s}$. The number density of subhalos per unit mass is defined as Einasto profile [4]

$$\frac{dn_{\mathrm{sub}}}{dM_{\mathrm{sub}}} = \frac{1}{3} c_0 \left(\frac{M_{\mathrm{sub}}}{m_0}\right)^n \exp\left(-\frac{2}{\alpha}\left[\left(\frac{r}{r_{-2}}\right)^\alpha - 1\right]\right) \tag{3.8}$$

with $n = -1.9$, $\alpha = 0.678$ and $m_0 = 2.52 \times 10^7 M_\odot$. The maximum impact parameter is set to $b_{\max} = 5r_s$ for a given subhalo mass. Following [26], the parameter c_0 is fixed to $c_0 = 2.02 \cdot 10^{-13} M_\odot^{-1}\,\mathrm{kpc}^{-3}$, and r_{-2} (for the MW) to $r_{-2} = 162.4\,\mathrm{kpc}$, where a prefactor of 1/3 is included to account for subhalo disruption by the baryonic disk. The total encounter rate is defined as [4]

$$\mathcal{R}(t) = \int_t^{t+\tau} dt' \int_{M_{\min}}^{M_{\max}} dM_{\mathrm{sub}}\, \sqrt{2\phi}\, \sigma_{\mathrm{sub}}\, \left|\vec{v}_s(t')\right| \times b_{\max}(M_{\mathrm{sub}})\, \frac{dn_{\mathrm{sub}}}{dM_{\mathrm{sub}}}(M_{\mathrm{sub}}, \left|\vec{r}_s(t')\right|) \tag{3.9}$$

Parameter	*Unit*	*Description*
t_{imp}	Gyr	Impact time
f_{imp}	-	Impact position, with $0 \leq f_{\mathrm{imp}} \leq 1$ along the stream
v_{sub}	km/s	Subhalo velocity
b	pc	Impact parameter
θ	rad	Polar angle
Φ	rad	Azimuth angle

TABLE 3.1: Kinematic impact parameters of the subhalo samples [4].

Bulge	
$M_{bulge}\ (M_\odot)$	4×10^9
$a_{bulge}(kpc)$	0.28
Disk	
$M_{disk}\ (M_\odot)$	5.5×10^{10}
$a_{disk}(kpc)$	3
$b_{disk}(kpc)$	0.28
Halo	
$M_{200}(M_\odot)$	1.08×10^{12}
$r_s(kpc)$	15.62

TABLE 3.2: Parameters for the MW bulge, disk and halo potentials [4].

3.1.2 Power Spectrum

3.1.2.1 Mathematical Description

Through the numerical implementation of the previous section, the positions of the stars in GD-1 after the subhalo impact are now determined. These positions can be divided into N bins x_i of equal size along the length of the stream[2]:

[2]The length of the stream can be described both by the Koposov coordinate ϕ_1 and by the physical length along the stream s.

$$x_i \in [x_{\min}, x_{\max}], \quad i = 0, \ldots, N-1 \tag{3.10}$$

In each bin x_i, the number of stars (= counts) is determined:

$$C_i = \text{counts per bin i} \tag{3.11}$$

Now, a fitting function can be applied on the counts in the bins. The underlying physical idea is to compare the perturbations in the stream (e.g., caused by a subhalo impact) to the undisturbed stream [26]. Following [71], a second-degree polynomial fit is used

$$f(x) = \sum_{\alpha=0} a_\alpha x^\alpha, \quad \alpha = 0, 1, 2 \tag{3.12}$$

The density in each bin can then be described by

$$\rho(x_i) = \frac{C_i}{f(x_i)}, \quad i = 0, \ldots, N \tag{3.13}$$

Subsequently, the Welch method is applied to the signal. Its two main steps are segmentation and windowing (see Subsubsec. ▶ 2.4.1.2). *Segmentation* (*Step 1*) means, that the signal is divided into M overlapping segments. By default, `csd` uses an overlap of 50 %, which means that the shift D between the segments is $D = L/2$. The segment length L (equal to `nperseg` in `csd`, see Subsubsec. ▶ 3.2.2.3) is the number of data points per segment. The number of segments is defined as [134]

$$M = \frac{N - L}{D} + 1 \tag{3.14}$$

In this analysis, the segment length L is set to N. This means that one segment corresponds exactly to one bin and effectively no segmentation takes place at all. While this leads to a higher variance in the power spectrum, it simultaneously results in a finer frequency resolution[3]. In this case, this is more important, as the analysis of density fluctuations along the GD-1 stream requires a high resolution. Therefore, the subsequence $\rho_m = (\rho_{mD}, \rho_{mD+1}, ..., \rho_{mD+L-1})$ in this case corresponds exactly to the bins. The second step of the Welch method is *windowing* (*Step 2*). This means, that a window function is applied. In this case, since $N = L$, this function is applied directly to the bins and smoothes the transitions between them. Per default, `csd` (see Subsubsec. ▶ 3.2.2.3) chooses a Hann-window:

$$w_j = 0.5 \left[1 - \cos\left(\frac{2\pi j}{L-1}\right)\right], \quad j = 0, \ldots, L-1 \tag{3.15}$$

[3] Because the frequency resolution is inversely related to the bin size.

This function is now multiplied with the subsequence of the segment to smooth the edges. The segments (in this case identical with the bins) can then be described as

$$s_j = w_j \cdot \rho_j, \quad j = 0, \ldots, N-1 \tag{3.16}$$

On this segment, the standard DFT is now applied (see Subsubsec. ▶ 2.4.1.1)

$$\tilde{s}_k = \sum_{j=0}^{N-1} s_j \cdot e^{-2\pi i \frac{kj}{N}}, \quad k = 0, \ldots, N-1 \tag{3.17}$$

The power spectrum is then

$$P_k = \frac{1}{U} |\tilde{s}_k|^2 \tag{3.18}$$

where U is the normalization factor of the window energy, given by

$$U = \frac{1}{N} \sum_{j=0}^{N-1} w_j^2 \tag{3.19}$$

The final step of the Welch method, averaging over all segments, in this case is not necessary, since the segments correspond exactly to the bins.

3.1.2.2 Coordinate Transformation

The length along the stream GD-1 can be described in two ways: The *angular coordinate* ϕ_1 and the *proper path length* along the stream. ϕ_1 originates from a coordinate system introduced by Koposov et al. [76], which was specifically tailored to the GD-1 stream. This system is a rotated spherical coordinate system (ϕ_1 = longitude, ϕ_2 = latitude)[4]. *Proper path length* s means the real physical length along the stream, described in [kpc]. As the distance of GD-1 is varying (see Subsubsec. ▶ 2.3.2.1), the transformation can be executed with the arc length formula

$$s(\phi_1) = \int_0^{\phi_1} \sqrt{1 + \left(\frac{\mathrm{d}D(\phi_1)}{\mathrm{d}\phi'_1}\right)^2}\, \mathrm{d}\phi'_1 \tag{3.20}$$

where D describes the heliocentric distance. As ϕ_1 is an angular coordinate, it is necessary to replace the differential length element $\mathrm{d}\phi_1$ with the physical length element $D\,\mathrm{d}\phi_1$, giving

$$s(\phi_1) = \int_0^{\phi_1} \sqrt{D(\phi_1) + \left(\frac{\mathrm{d}D(\phi_1)}{\mathrm{d}\phi'_1}\right)^2}\, \mathrm{d}\phi'_1 \tag{3.21}$$

[4]For the transformation matrix from (α, δ) to (ϕ_1, ϕ_2), see [76].

3.2 Numerical Implementation

Now, that the theoretical concepts are clear and the physical model has been established, the task can be implemented numerically. The main code consists of two parts: *Part 1, Stream Simulation*, was written by Prof. Sean Tulin and adapted by myself for the special tasks. *Part 2, Power spectrum*, was mainly written by myself on the base of a Jupyter notebook by Elham Rahimi. The power spectrum part of the code is available on GitHub and can be accessed with the link ▶ Ocean16151/stream-team-power-spectrum. Subsubsection ▶ 3.2.1.2 describes the structure and modular design of the code, Subsection ▶ 3.2.2 the implementation of the steps within the code, and Subsection ▶ 3.2.3 its execution. The individual steps are also linked on GitHub[5].

The procedure was as follows: First, a test version for the power spectrum was developed in order to reproduce the results of [71]. Subsequently, the two base codes were aligned and prepared for analysis. Later, various modified versions were created. All codes were initially developed as *Jupyter Notebooks* and then converted into *Python* scripts, which were executed on the cluster computer of the Institute for Theoretical Physics of Goethe University, Frankfurt, via *Bash scripts* (see Subsubsec. ▶ 3.2.3.2). The final plots were created using a separate *Jupyter Notebook*.

3.2.1 Programming Framework and Code Organisation

3.2.1.1 Python and the `csd` Algorithm

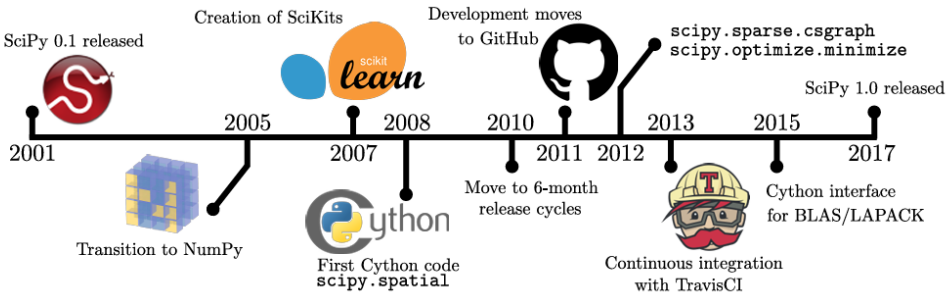

FIGURE 3.2: Important milestones in the development of the `SciPy` library: Since 2005, `SciPy` has been based on the `NumPy` library, which emerged from its predecessors `Numeric`, and `Numarray`. Other libraries used in this work include `SymPy` (for symbolic computation, since around 2006), `pandas` (for table-based data processing, since 2008), `matplotlib` (for plotting, since 2003), and `math` (mathematical functions, since 1995) [131].

[5]These links refer to the Jupyter Notebook of the main version of the power spectrum code.

The code is written in Python, a programming language that was developed with the aim to enable a simple and highly readable programming style [107][6]. Python aligns well with the requirements of transparency, reproducibility, and accessibility in astrophysics, and is therefore widely used. Its modular structure has enabled the development of numerous libraries specifically tailored to astronomical data processing, such as `Astropy` [6]. To compute the *power spectrum*, the signal processing suite `scipy.signal.csd` (`csd`) was used. `csd` is a part of the SciPy software framework, a scientific Python library founded by Eric Jones and Travis Vaught in 2001 [131] (see Fig. 3.2, showing important stages of the development of the project). The `scipy.signal` module includes classical signal processing tools such as filters, spectral analysis methods, and window functions. The `csd` function belongs to the spectral analysis suite and was developed around the same time as the functions `welch`, `coherence`, and `spectrogram`. Within this analytical framework, `csd` represents a generalization of welch, as it can estimate not only the auto power spectrum S_{xx} (f), but also the cross power spectrum S_{xy} (f). Additionally, it is possible to select whether a power spectrum or a PSD should be computed.

3.2.1.2 Code Structure and Modular Design

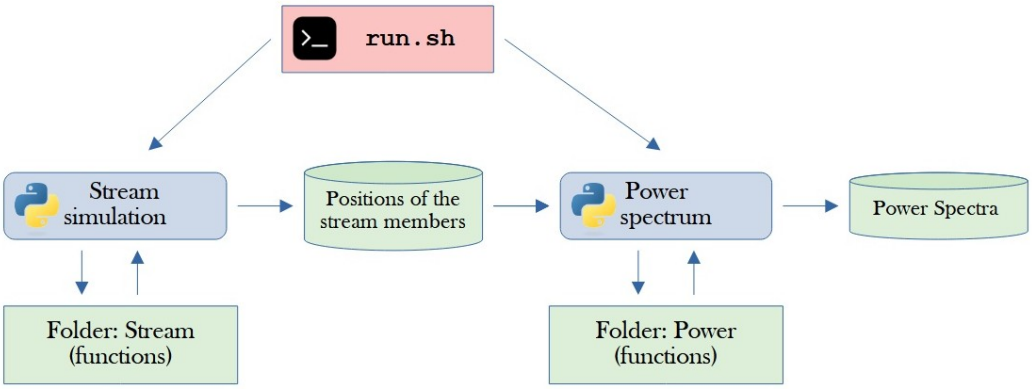

FIGURE 3.3: This figure shows the *folder structure* of the code. The central components are the two main scripts, `Stream simulation` and `Power spectrum`, each with their own associated folder systems containing the relevant functions. The output of the first script, the *stream simulation*, includes both a visual representation and the positions of the individual member stars of the GD-1 stream, and is read by the second script. This script then computes a power spectrum as a function of both ϕ_1 and s.

Figure (3.3) shows the steps of the computation: *Part 1, Stream Simulation* (see Subsubsec. ▶ 3.2.2.1) first performs the simulation of the subhalo impact on the stream.

[6]The name originates from the fact that the creator was a big fan of *Monty Python's Flying Circus* [82].

As output, the code provides the positions of the stream stars after the subhalo impact. *Part 2, Power Spectrum*, then reads in this output from the first part and calculates the power spectra as function of ϕ_1 and s respectively. Each code has an associated folder structure containing its respective functions. For the Stream Simulation code, this is the `stream` folder; for the Power Spectrum code, it is the `power` folder. Due to the modular building-block design, core operations such as binning or fitting can be applied multiple times, as demonstrated in Figure (3.6) (see Subsubsec. ▶ 3.2.2.2). The codebase presented here provides the framework for a single run at a time. The number and type of iterations were therefore controlled with the Bash script (see Subsubsec. ▶ 3.2.3.2). The communication between Bash script and the two main codes was handled through the environment variable `num_data`. Regarding the choice of the subhalo profile, both codes were designed such that the profile needed to be specified only once at the beginning of the code, after which the rest of the code would automatically adapt accordingly.

3.2.2 Code Modules

3.2.2.1 Stream Simulation

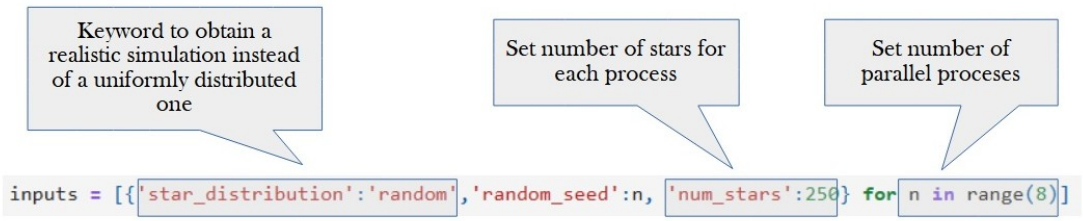

FIGURE 3.4: Input interface of the `multiprocessing` tool. The desired number of stars per simulation can be controlled via both the number of parallel processes and the number of stars per process. The number of processes was chosen to match the number of parallel nodes requested in the Bash script.

Part 1 of the code, *Stream Simulation*, is based on the package `stream`, which provides numerous tools for simulations with the GD-1 stream. The two modules used in this code are, first, `stream.simulate()`, which outputs a list of phase space trajectories for N stars, and second, `coordinates`, which allows conversions between galactocentric coordinates and various celestial positions (e.g., ϕ_1 and ϕ_2, see Subsubsec. ▶ 3.1.2.2). To generate a realistic version of the stream, the `multiprocessing` tool (see also Subsubsec. ▶ 3.2.3.2) can be employed. In this tool, a few keywords can be set, as Figure (3.4) shows. To simulate a specific number of stars, both the number of parallel processes and the number of stars per process can be freely chosen. To reduce computation time, the number of parallel processes was matched to the number of cores used on the

ITP cluster (see Subsubsec. ▶ 3.2.3.2). The number of stars was set to 2000 in all simulations. Figure (3.5) shows the example of the output, a simulated version of GD-1 for the subhalo with `num_data` = 44.

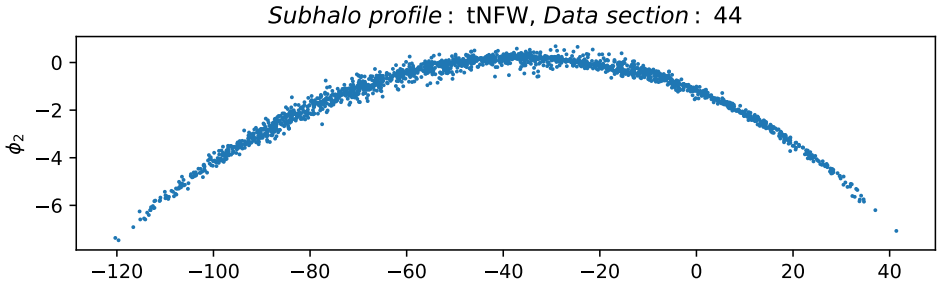

FIGURE 3.5: Example of an output of the stream simulation. The stellar positions were plotted as a function of the Koposov coordinates (ϕ_1, ϕ_2).

For comparison, also a version with a bootstrap sampling was run. Bootstrap sampling means, that a new sample of the same size is repeatedly drawn with replacement from the original dataset. Like this, several random realisations of the stream simulation could be performed.

3.2.2.2 Power Spectrum: Structure

Part 2, Power Spectrum, consists of three modules, which are introduced in the following sections: calculation of the power spectrum (I), conversion from the ϕ_1 Koposov coordinate to the physical length along the stream, s (II), and plotting of the power spectrum (III). These are organized into three distinct blocks: the calculation of the power spectrum as a function of ϕ_1 (a), the coordinate transformation (b), and the determination of the power spectrum as a function of s (c). Figure (3.6) illustrates the structure of the code, including which functions from the modular system are used in each step. The procedure is as follows: first, the stars are assigned to a binning scheme along the ϕ_1 coordinate. The same binning scheme, aligned with [71], was used. Using a fit, the density per bin can then be determined. Subsequently, the power spectrum is calculated using the `csd` algorithm and plotted. Afterwards, the conversion from the angular coordinate ϕ_1 to the physical length s along the stream is implemented (for a detailed description of the steps, see Subsubsec. ▶ 3.2.2.5). The calculation of the power spectrum as function of s follows the same procedure as for ϕ_1.

3.2.2.3 Power Spectrum I: Computation with `csd`

As indicated above, the first operation to perform was the binning of the counts along the stream (see ▶ Power Spectrum, main, Cell 7) and the fitting of the histogram in accordance with Equation (3.12) (see ▶ Power Spectrum, main, Cell 10). The number

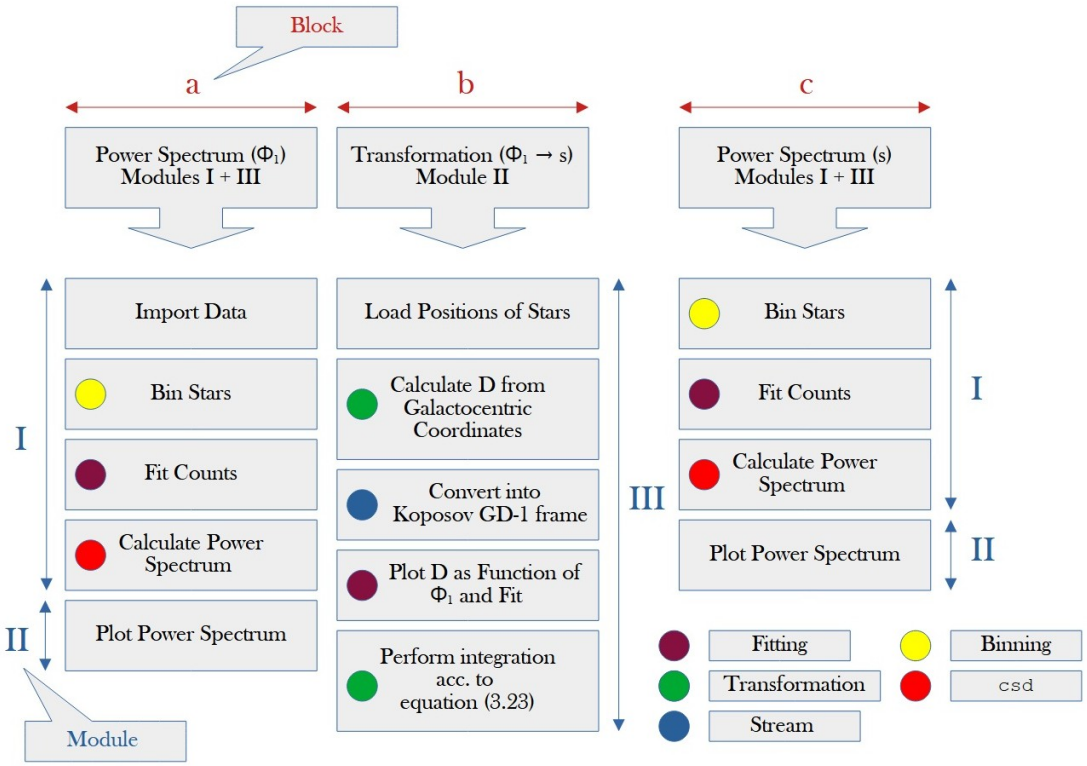

FIGURE 3.6: Structure of the Power Spectrum code. It consists of three modules, which correspond to the following subsubsections of this thesis: computation with `csd` (I), plotting and normalization (II), and unit transformation (III). Colored dots indicate the functions used in each step. These originate from the modules fitting (purple), binning (yellow), transformation (green), and the `stream` folder, which belongs to the stream simulation code (blue). The `csd` algorithm from `scipy` is marked in red. The three blocks of the code are represented using lowercase letters.

of bins was set to $N = 40$ troughout the analysis, following [71]. The density per bin could now be calculated with Equation (3.13). Subsequently, the power spectrum could be determined with the `csd` algorithm (see ▶ Power Spectrum, main, Cell 13). Figure (3.7) shows the input parameters of the `csd` algorithm, where the following parameters are set:

- *Sampling frequency* f_s: The sampling frequency (= the number of data points per unit length) is set to 1 devided by the size of each bin. This is necessary to ensure that the resulting frequency axis has a meaningful physical unit of $[1/°]$, allowing inverse frequencies $1/f$ to be interpreted as angular scales along the stream.
- *Window*: A `Hann window` is chosen per default (see Eq. 3.15).

- *Scaling*: Selecting `spectrum` instead of `density` ensures that a *power spectrum* is computed rather than a *PSD*. Instead of giving the power per unit frequency (as PSD does) the power spectrum returns the total power in each frequency bin.
- *Number of samples per segment*: `nperseg` defines the number of consecutive data points used to form each segment of the signal for individual spectral estimation. In this analysis nperseg is set to 40 which corresponds to len(signal). This means, that no segmentation or averaging is performed, which means the variance of the spectral estimate is not reduced. However, this approach is advantageous when the highest frequency resolution is required, as dividing the signal into smaller segments would broaden frequency bins and diminish spectral detail. It is particularly suitable for analyses where preserving fine spectral features and direct comparison to theoretical models is important, despite the increased variance in the estimate.

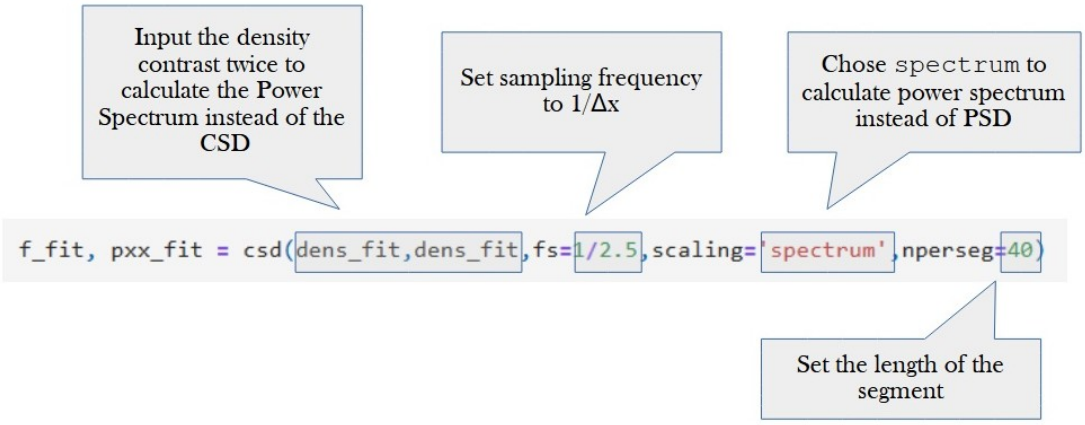

FIGURE 3.7: Input structure of `csd`: By providing the same array (`dens_fit`) as both inputs, the power spectrum ($S_{xx}(f)$) is computed instead of the cross spectral density ($S_{xy}(f)$). The sampling frequency is set to $1/bin - size$, since the power spectrum is plotted against the inverse of frequency. By setting `nperseg = 40`, which corresponds to the total number of bins used in the analysis, no segmentation is performed by `csd`.

3.2.2.4 Power Spectrum II: Plotting and Normalisation

The plotting approach follows Bovy et al. [26, 27]. The x-axis shows the inverse frequency $1/f$, which corresponds to the spatial scale of the fluctuations. The power is normalized by the total length of the considered stream segment. The power spectrum thus describes the strength of fluctuations at different spatial scales $1/f$, averaged over

the full length of the stream. This normalization is essential to make results comparable across stream segments of different lengths. Without it, the total number of possible fluctuations per unit length and hence the amplitude of the spectrum would depend on the total length and distort the comparison. In the plot (see ▶ Power Spectrum, main, Cell 16), the square root of the power is plotted in order to display the *amplitude* rather than the *power* itself (compare with Eq. 2.29). A *double logarithmic plot* finally makes it possible to visualize wide value ranges and allows for greater comparability. For the power spectrum as function of s, the same procedure is applied (see ▶ Power Spectrum, main, Cell 39).

3.2.2.5 Power Spectrum III: Coordinate Transformation

To compute the power spectrum as a function of s using the same procedure as just described, the density contrast needs to be derived as function of s. The transformation according to Equation (3.21) therefore needs to be implemented numerically. To accomplish this, two different approaches were used troughout the analysis. In the *test version* (*Method 1*), random star positions were first generated based on the counts in each bin of the counts as function of ϕ_1. These positions were subsenquently transformed into s-values following Equation (3.21). To determine the heliocentric distance D, a formula provided by [71] was used:

$$D(\phi_1) = -4.302\,\phi_1^5 - 11.54\,\phi_1^4 - 7.164\,\phi_1^3 + 5.985\,\phi_1^2 + 8.595\,\phi_1 + 10.36 \tag{3.22}$$

The integration was performed numerically, using the `ode.solver` by `scipy` (see Fig. 3.2). These s-values were binned (with start, end and bin-size according to [71]). This method is only accurately applicable to the reference data from [71], since the heliocentric distance as a function of the position ϕ_1 along the stream differs between the various stream simulations. In the *main version and modifications* (*Method 2*), to be applicable to different versions of the stream, Equation (3.22) had to be recalculated and adjusted. For this purpose, the heliocentric distance D was initially derived from the galactocentric coordinates of the GD-1 member stars

$$D = \sqrt{(x - x_0)^2 + (y - y_0)^2 + (z - z_0)^2} \tag{3.23}$$

The positions of the member stars as a function of ϕ_1 were determined using the `coordinates.transform` function from the `stream` folder. The heliocentric distance D of the stars could then be plotted as a function of ϕ_1, as shown in Figure (3.8) for a single dataset (see ▶ Power Spectrum, main, Cell 25). Using a quintic polynomial fit, an equation equivalent to Equation (3.22) could thus be constructed (see ▶ Power Spectrum, main, Cell 23). The remaining steps are analogous to *Method 1.* Figure (3.8)

shows the heliocentric distance as function of the angular coordinate ϕ_1 according to Equation (3.22) (left side) and the own computation (right side).

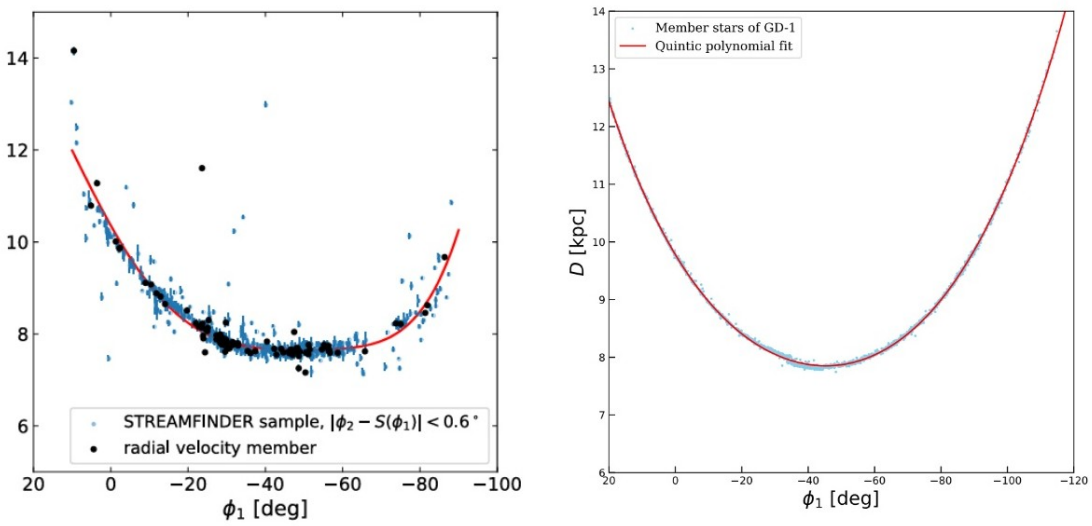

FIGURE 3.8: *Heliocentric distance D* as function of ϕ_1 from [71] (left) and the own data (right). The plot also shows how far away GD-1 is from us (respectively the sun) in different angular sections. This reveals, that the stream is several kpc closer to the sun (and thus to the earth) near its center.

3.2.3 Execution

3.2.3.1 Technical Setup of the ITP Cluster

For the execution, the own cluster computer at the Institute of Theoretical Physics, Goethe University Frankfurt, was used. A cluster computer is a networked system of multiple computers working together as a single (high-performance) machine. Characteristics of a cluster include that it consists of many individual computers (called *nodes*), which often have specialized roles (e.g. controllers that manage the cluster, compute nodes that perform calculations, and storage nodes that handle data storage). These nodes are connected via a high-speed network. The ITP cluster is centrally managed by a specialized software, called *slurm*. Figure (3.9) shows the architecture of this software. A central element is the so-called *controller daemon*[7], which is a specialized background process responsible for centrally controlling, coordinating, and monitoring the system. As illustrated in Figure (3.9), the main controller daemon in slurm is called `slurmctld`. This system coordinates the entire cluster, decides which jobs run on which nodes, communicates with `slurmd` processes on the compute nodes, monitors resources, and

[7] A *daemon* in software or an operating system is a background process that runs automatically and performs specific tasks without being started or directly controlled by a user [7].

responds to changes in system state. Furthermore, it coordinates the user commands (e.g. `sbatch` to execute a bash script). The `slurmd` daemons (see Fig. 3.9) on the individual nodes regularly report their status (e.g. source usage, job progress) back to `slurmctld` [116].

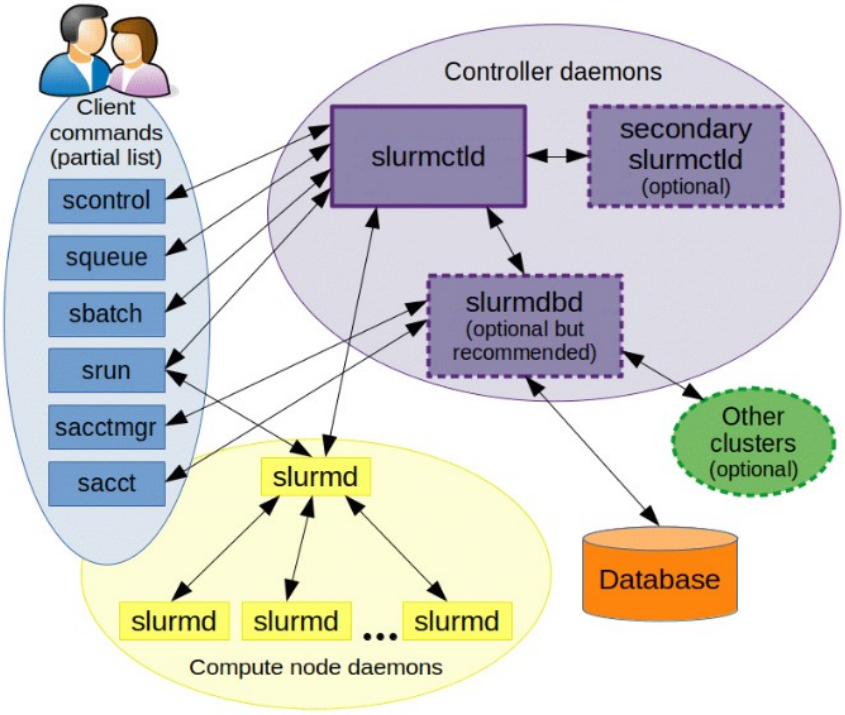

FIGURE 3.9: Architecture of *slurm*. The `slurmctld` is the central manager that organizes resources and work. Each connected individual computer (node) runs its own `slurmd` daemons [7], which are comparable to a remote shell. Possible commands a user can enter in the shell include `srun` (= execute jobs), `sbatch` (= run a Bash script), and `squeue` (= display jobs currently in progress) [116].

3.2.3.2 Bash Scripts

The *Bash scripts* were individually adjusted and tailored for each run of the code. An important task of them was to manage the iteration and the choice of the subhalo samples. A central question was how to carry out the computationally intensive calculations, especially due to the large number of iterations, in the fastest way[8]. Therefore, also the use of *Message Passing Interface (MPI)* [61] was considered. This is a standard for parallel programming that allows multiple processes to run simultaneously and communicate with each other, typically used on high-performance computing clusters. In a

[8]This was particularly relevant for the *stream simulation* in *Part 1*, which was the most time-consuming part of the process.

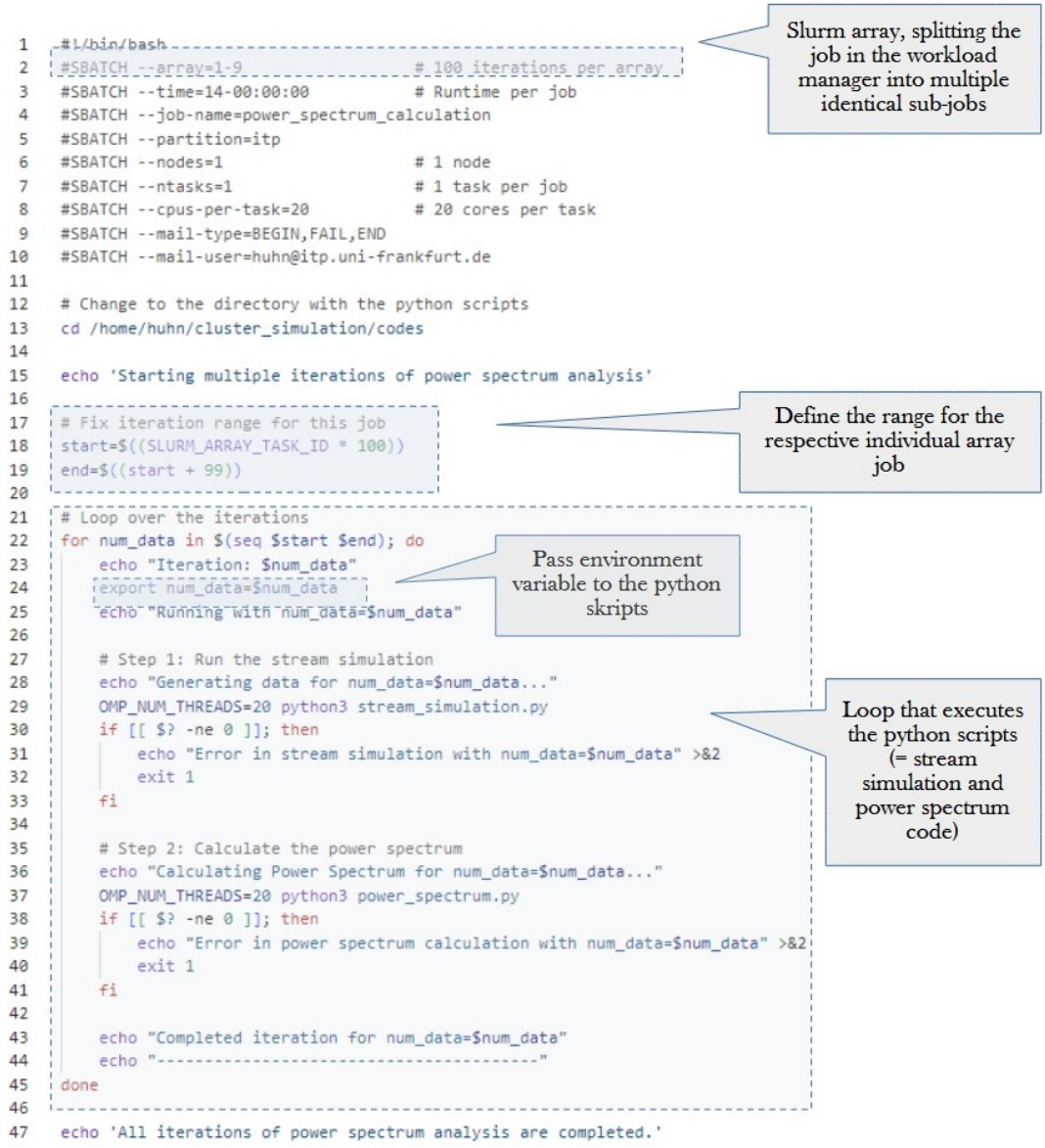


```
#!/bin/bash
#SBATCH --array=1-9                    # 100 iterations per array
#SBATCH --time=14-00:00:00             # Runtime per job
#SBATCH --job-name=power_spectrum_calculation
#SBATCH --partition=itp
#SBATCH --nodes=1                      # 1 node
#SBATCH --ntasks=1                     # 1 task per job
#SBATCH --cpus-per-task=20             # 20 cores per task
#SBATCH --mail-type=BEGIN,FAIL,END
#SBATCH --mail-user=huhn@itp.uni-frankfurt.de

# Change to the directory with the python scripts
cd /home/huhn/cluster_simulation/codes

echo 'Starting multiple iterations of power spectrum analysis'

# Fix iteration range for this job
start=$((SLURM_ARRAY_TASK_ID * 100))
end=$((start + 99))

# Loop over the iterations
for num_data in $(seq $start $end); do
    echo "Iteration: $num_data"
    export num_data=$num_data
    echo "Running with num_data=$num_data"

    # Step 1: Run the stream simulation
    echo "Generating data for num_data=$num_data..."
    OMP_NUM_THREADS=20 python3 stream_simulation.py
    if [[ $? -ne 0 ]]; then
        echo "Error in stream simulation with num_data=$num_data" >&2
        exit 1
    fi

    # Step 2: Calculate the power spectrum
    echo "Calculating Power Spectrum for num_data=$num_data..."
    OMP_NUM_THREADS=20 python3 power_spectrum.py
    if [[ $? -ne 0 ]]; then
        echo "Error in power spectrum calculation with num_data=$num_data" >&2
        exit 1
    fi

    echo "Completed iteration for num_data=$num_data"
    echo "----------------------------------------"
done

echo 'All iterations of power spectrum analysis are completed.'
```

FIGURE 3.10: One of the bash scripts as example. The time is set to the maximum allowable interval of 14 days on the ITP cluster and the number of CPUs per task is adjusted to the number of parallel processes in the `multiprocessing` tool, used in the stream simulation code. In the *main part*, the main loop calls, for each iteration, both part 1 (Stream Simulation) and part 2 (Power Spectrum). In each case, the environment variable `num_data` is passed to the codes.

slurm job, MPI enables a program to be distributed across several CPUs or nodes using commands like `srun` or `mpirun`. This allows tasks to be executed in parallel rather than sequentially. It is particularly useful for complex computational tasks where coordination between processes is required to exchange data or status information. However,

when processes are fully independent, as it was the case in this analysis, no inter-process communication is necessary. Therefore, dividing the jobs into different slurm *arrays* and assigning a suitable number of individual iterations per array (typically 100) proved to lead to a good balance between the load on cluster resources and the runtime of a single array job. Figure (3.10) shows an example of such a bash script that was used for the computations. It illustrates how the individual iterations are invoked using a loop and distributed across different array jobs. During each run, an environment variable (`num_data`, see also Subsubsec. ▶ 3.2.1.2) is passed to the Python codes, choosing the corresponding sample subhalo in the stream simulation code. This environment variable is labeled consistently throughout the entire codebase, ensuring a clear association of each intermediate step and result with its respective subhalo[9]. To ensure the highest possible efficiency and to avoid potential performance degradation due to resource contention, the `multiprocessing` tool (see Subsubsec. ▶ 3.2.2.1) was referenced and the number of parallel processes aligned with the number of allocated CPU cores.

3.2.3.3 Plots

The plots presented in this work were each generated using a separate *Jupyter Notebook*. For this purpose, the data from a single iteration were saved to a file, using the environment variable `num_data` to indicate the run (see Subsubsec. ▶ 3.2.1.2). All iterations were then combined in the plotting routine. The plots shown for each model represent the *median* value across all iterations. The shaded regions indicate the range between the 16th and 84th percentiles, calculated from the full set of iterations.

[9]This was important, as the computations, performed with different variants over time, produced a large volume of data and results.

Chapter 4

Results

4.1 Power Spectra

4.1.1 Main Version

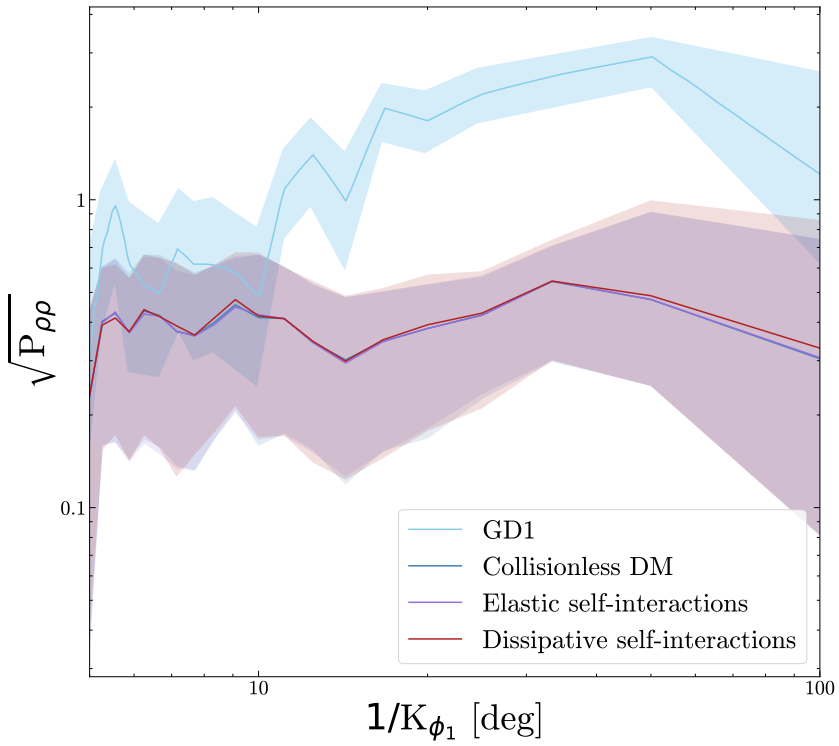

FIGURE 4.1: This figure shows the density power spectrum as a function of ϕ_1 for the three models considered. Shown are the *median* value and the range between the 16th and 84th percentiles for a total of 1000 iterations. For comparison, the power spectrum of GD-1 is included (bright blue) (from [71]).

Figure (4.1) shows the results for the three different models as a function of ϕ_1. Only subhalos with an impact time of $t_{\text{imp}} < 2\,\text{Gyr}$ are taken into account. Shown are the median values along with the 16th to 84th percentiles in comparison with the power spectrum of GD-1 (from [71], bright blue). It can be observed that a plateau forms, beginning at $1/k_{\phi_1} = 20°$. The results from our own simulations for the different models show a more uniform behavior, with a slight peak around $\Delta\phi_1 = 30°$ and no significant difference between the models. A similar picture emerges for the power spectrum as a function of s. A clear peak can now be seen in the spectrum of GD-1 (bright blue, [71]) at $s \approx 2.6\,\text{kpc}$. This roughly corresponds to a separation of $\phi_1 = 20°$ in the Koposov angular coordinate system[1]. Again, no difference between the models is observable and a distinct minimum appears at the position $s \approx 2.6\,\text{kpc}$.

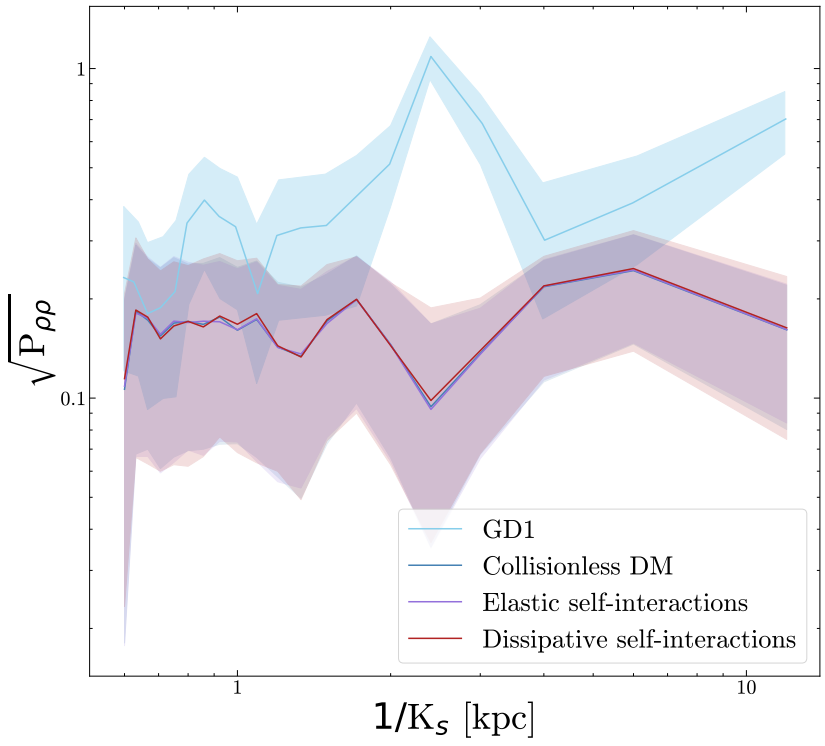

FIGURE 4.2: This figure shows the density power spectra of the different models as a function of s, calculated with the same method as in Figure (4.1). The power spectrum of GD-1 (light blue) clearly exhibits a characteristic peak at $s = 2.6\,\text{kpc}$, while the power spectra from the simulations display a minimum at precisely this scale.

[1]The conversion can be roughly estimated using the formula $s = D \cdot \Delta\phi_1 \cdot \frac{\pi}{180}\,[\text{kpc}] = 8 \cdot 20 \cdot \frac{\pi}{180}\,[\text{kpc}] \approx 2.79\,\text{kpc}$, where D is the heliocentric distance. It is taken into account that the heliocentric distance of GD-1 is lowest near the central region.

4.1.2 Bootstrap Version

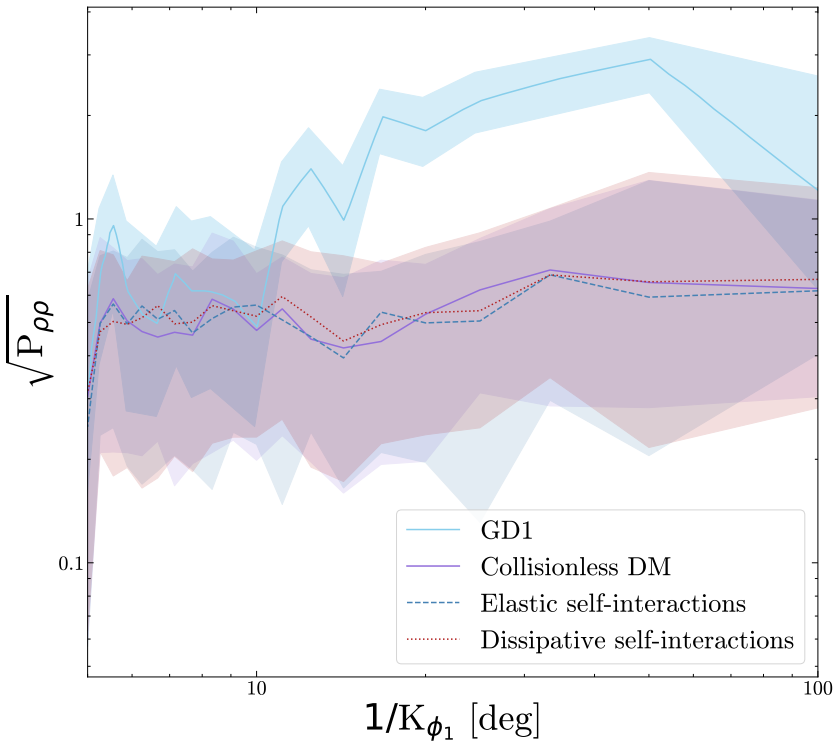

FIGURE 4.3: This figure shows the density power spectrum as a function of ϕ_1 for the three models considered. A bootstrap sampling was now applied to the stream simulation. Shown are again the *median* value and the range between the 16th and 84th percentiles for a total of 100 iterations.

Figure (4.3) shows the density power spectrum as a function of ϕ_1. A bootstrap sampling was applied to the star positions from the stream simulation (see Subsubsec. ▶ 3.2.2.1). The different models now differ slightly from each other, but no systematic trend is apparent. In the power spectrum as a function of s (see Fig. 4.4), the minimum at $s = 2.6\,\mathrm{kpc}$ is now significantly less pronounced. This could indicate that there is a systematic cause for it (see Sec. ▶ 4.2). The slight differences now emerging between the models could be attributed, on the one hand, to the stochastic influence of the bootstrap sampling and, on the other hand, to the reduced number of iterations by a factor of 10.

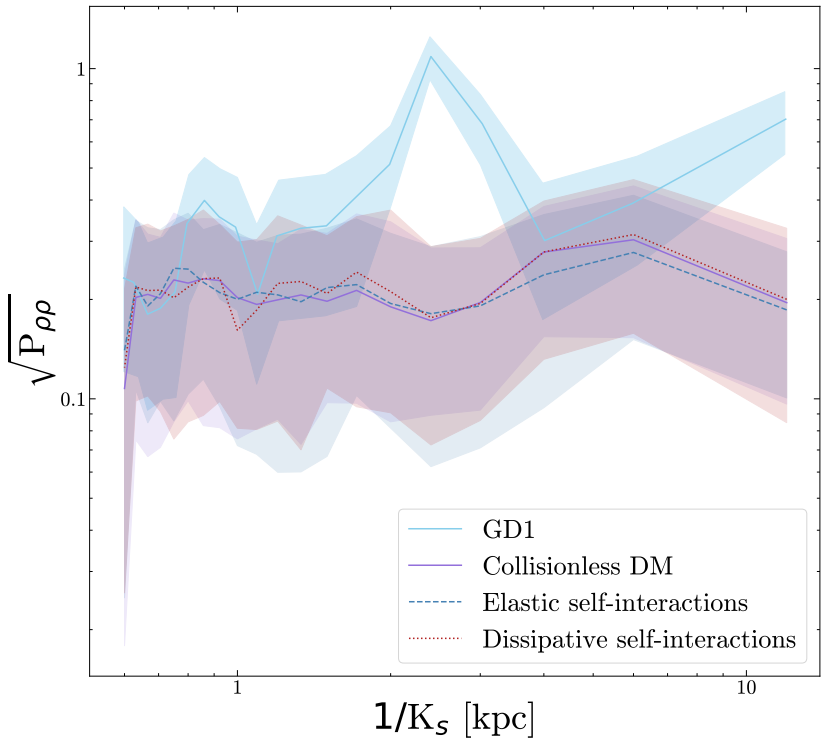

FIGURE 4.4: This figure shows the density power spectrum as function of s, with a bootstrap sampling applied on the stream simulation. The plot shows the *median* value and the range between the 16th and 84th percentiles for a total of 100 iterations.

4.2 Discussion

4.2.1 Gap and Epicyclic Patterns

To put the results into context, it is useful to first revisit the discussion on the origin of the gap at $\phi_1 = 40°$ hinted at in Section ▶ 2.3.2.3. While Bonaca et al. [19] provide a detailed argument that a subhalo impact is the most likely cause of the gap, Ibata et al. [71] point out, that the gap could as well be a part of the epicyclic stream-fanning pattern. This is a consequence of GD-1 having formed from a GC, as described above (see Subsubsec. ▶ 2.3.1.1). [71] emphasize that there are no unambiguous, distinctive impact signatures that can only be caused by a subhalo. The feature that [19] put forward as the main argument for a massive object impact causing the gap at $\phi_1 = 40°$ is interpreted by [71] as a geometric part of the stretched stellar stream. The density power spectrum, as described in this work, is an important tool in this context to

reveal regular patterns, such as the epicyclic overdensities and underdensities. Due to the formation process of GD-1 from a GC, this pattern is not random but exhibits a periodic structure. The peak, which is especially pronounced in the spectrum as a function of the proper path length s, is significant here as it reflects the periodic length. Its value lies at $1/k_s = 2.64 \pm 0.18\,\mathrm{kpc}$ and was extracted by the power spectrum of GD-1 (see Fig. 4.2) [71]. This distance, which corresponds to approximately $s \approx 20°$, matches exactly the separation between the two gaps at $\phi_1 = -20°$ and $\phi_1 = -40°$, which [71] cite as further evidence for a geometric origin. Nevertheless, there are strong arguments in favor of a DM subhalo as the cause, as discussed above (see Subsubsec. ▶ 2.3.2.3).

4.2.2 Limitations

However, the question arises whether a density power spectrum is an optimal tool for this particular case. Since this scenario does not involve a regular pattern along the entire stream, but rather the the effect of a subhalo impact, the result will at least be affected by other density fluctuations. Another relevant question is whether the density power spectrum, as constructed here, is in principle capable of capturing subhalo impacts. Given the total considered stream length of nearly 100° and the use of 40 bins, each bin corresponds to an angular section of 2.5°. The Nyquist limit, which is the smallest resolvable structure, is therefore $\lambda_{\mathrm{min}} = 2 \cdot \Delta\phi = 5°$ [95][2]. Most studies adopt gap widths of less than $\phi_1 < 10°$ in their models (e.g., [19]), implying that a subhalo impact should in principle be detectable at this resolution. However, it remains questionable whether the more subtle differences caused by variations in the density profile of individual models can be captured in this setup. Even if this were possible, the full length of the stream is still included in the analysis, making it likely that more precise methods would be preferable. Finer binning or focusing on a smaller section of the stream are, in principle, possible alternatives. However, doing so reduces the spectral resolution, which introduces its own limitations. This could explain why differences between the models are practically not visible in this setup.

4.2.3 Systematic Effects

Finally, the question arises why the maximum in the GD-1 power spectrum as a function of s (see Fig. 4.2) appears to be mirrored across the x-axis in the simulation data. The code was designed to approximately reproduce the result of [71]. However, the streams simulated in Part 1 of the code do not reproduce the density profile of GD-1 in detail, so

[2]This follows from the method used to compute the power spectrum, which, as described (see Subsubsec. ▶ 2.4.1.1), is based on a DFT of the density along the stream. In order to recognize a sinusoidal oscillation, at least two data points per period are required.

an identical result was not expected. At first glance, this mirroring is therefore rather surprising. The results of the bootstrap simulation, in which stochastic processes also influenced the outcome and the minimum is much less pronounced, suggest that there may indeed be a systematic origin for this effect. In principle, this effect could arise from a phase shift, such as one caused by a shifted binning. However, to produce exactly this inversion pattern, the phase would need to be shifted by half a period, which corresponds to about four bins. In the simulation, however, the exact binning from [71] was used. A cumulative effect can also be ruled out, since the stellar positions as a function of s were calculated independently from the power spectrum as function of the angular coordinate. A possible explanation might be, that the simulated streams exhibit a different density profile than GD-1. Therefore, the minimum could maybe appear as a negative contrast. Further work is planned to revisit and refine these results.

Chapter 5

Conclusion and Outlook

In this work, density power spectra were calculated along the GD-1 stellar stream to investigate the influence of DM subhalo impacts under different DM models. No significant difference between the various models was found. It is possible that the density power spectrum is not an optimal tool to precisely capture the effects of different density profiles arising from various DM models (see Subsec. ▶ 4.2.1). Nevertheless, the determination of the power spectrum was very helpful in validating the method. Furthermore, the code is available and can be used to analyse other density profiles. Future work is planned to revisit and refine these results, which represent only an intermediate step. Additionally, a paper summarizing the complete findings of the Stream-Team project sis currently in preparation. Also in the future, stellar streams will remain valuable tools for probing the properties of DM. In order to be suitable for constraining DM by considering possible subhalo impacts, stellar streams should ideally exhibit the characteristics discussed in this work. In particular, they should have a sufficient distance from the Galactic bulge. Moreover, it is advantageous if the streams are narrow and well-resolved in observational data (see Subsubsec. ▶ 2.3.2.1). Alongside GD-1, Palomar 5 is considered a promising candidate for DM constraints [55]. It shows significant underdensities and asymmetries (see [56]) and exhibits very narrow, kinematically cold structures stretching over 20° across the sky, with a width of only 0.7° [135]. Studies (see e.g. [10]) have shown that density gaps within Palomar 5 may have been caused by both DM subhalos and baryonic structures. A detailed investigation of these gaps could therefore represent a promising approach to probing the nature of DM [100]. Other streams, like ATLAS [18], have so far not been mapped as well, or like Jhelum [17], where a lack of a clear epicyclic structure makes the analysis more difficult. Nevertheless, it could be an exciting idea for the future to identify further objects and continue to develop new techniques to make DM visible. Already now, a big variety of approachs is used (see e.g. [25, 18]). Even though, to close this journey by returning to the beginning, we still perceive DM only as a shadow on the wall, it is well worth continuing to explore this fascinating subject. Perhaps one day, humanity will be able to grasp its nature and rediscover itself beneath the wide and beautiful sky of reality.

Appendix A

Theoretical Supplements

A.1 Derivation of the Composition of the Universe

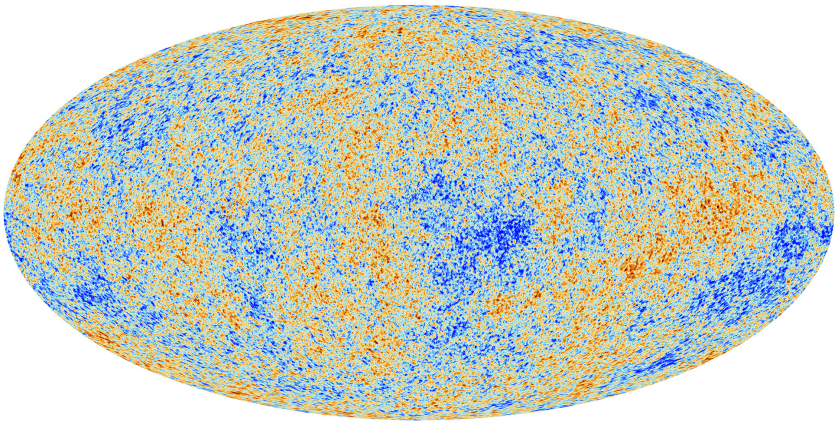

FIGURE A.1: The *oldest photo of the universe*: The cosmic microwave background (CMB). This visualisation shows the temperature fluctuations in the early universe as tiny variations in color. These anisotropies reflect regions of slightly higher or lower density. The different colors represent warmer (orange) and colder (blue) regions. The overall temperature of the CMB is approximately 2.725K. The shown temperature fluctuations are only a tiny fraction of that, on the order of $\Delta T/T \approx 10^{-5}$. The representation of the entire sky (= *all-sky map*) in elliptical form is called a *Mollweide projection.*

The CMB was accidentally discovered by Arno Penzias and Robert Wilson in 1965 [103] and can be considered as the *oldest photo* of the universe (Fig. A.1). It can be used to determine the composition of the universe. The moment when the CMB was formed, the *recombination*, was the time when electrons and protons combined to form neutral hydrogen. This made the universe transparent for the first time, allowing photons to travel freely through space. The CMB is indeed electromagnetic radiation (= mediated by photons), but in the microwave range because the originally very short wavelength has been greatly stretched due to the expansion of the universe (= redshift), so that it can now be measured as microwave radiation (hence the name *microwave background*).

The CMB can be used to determine the composition of the universe. For the wavelength in a contracting universe, the following applies:

$$\frac{\lambda_0 - \lambda_e}{\lambda_e} = \frac{1-a}{a} \tag{A.1}$$

with the scale factor of the universe a, the wavelength at emission λ_e, and the wavelength at observation λ_0. With $T \propto 1/\lambda$ follows

$$\frac{T_0}{T} = a \tag{A.2}$$

As the light has been emitted by a black body at 3000K and the universe has expanded since then by approximately factor 1100, a black-body radiation at $T \approx 2.73\,\mathrm{K}$ is resulting. The cosmic background radiation is, however, not completely uniform, but shows temperature fluctuations on the sky on the order of

$$\frac{T}{T} \approx 10^{-5} \tag{A.3}$$

These anisotropies reflect density variations in the early universe and form the basis of the structures we observe today. The temperature fluctuations on the sky are described by a function T in the direction $\hat{n}$, which can be decomposed into spherical harmonic functions Y_{lm}.

$$T(\vec{x}, t, \vec{\hat{n}}) = T_0 \sum_l \sum_{m=-l}^{l} a_{lm}(\vec{x}, t) Y_{lm}(\vec{\hat{n}}) \tag{A.4}$$

The coefficients a_{lm} of this decomposition contain the information about the anisotropies. The multipole number l roughly corresponds to the angular resolution, with an angle scale approximately given by $\theta \approx \pi/l$.

$$\langle a_{lm}(\vec{x}, t) a^*_{l'm'}(\vec{x}, t) \rangle = \delta_{ll'} \delta_{mm'} C_l(t) \tag{A.5}$$

The transfer function $\Theta_T(k, \ell)$ can be derived by solving the Einstein and Boltzmann equations. The spectrum today can then be expressed by

$$\frac{l(l+1)C_l}{2\pi} = \int \Theta_T^2(k, \ell) \mathcal{P}(k) \frac{dk}{k} \tag{A.6}$$

By decomposing the actually observed temperature fluctuations into spherical harmonics a_{lm}, the currently observed power spectrum can be extracted. As the transfer function $\Theta_T(k, \ell)$ depend on the density parameters trough various effects of cosmological perturbation (e.g. the Bardeen potentials, the Sachs-Wolfe effect or the Silk damping), the

result obtained by varying this parameters can be compared with the real observation. From this, the composition of the universe can finally be derived [51].

A.2 Derivation of the Thermodynamic Description

In this section, Equation (2.25) is derived following [24]. The second law of thermodynamics states that

$$TdS = dQ \tag{A.7}$$

It can also be expressed, as a function of the specific entropy s, as

$$T\left(\frac{\partial s}{\partial t}\right)_M = \frac{1}{\rho V}\left(\frac{dQ}{dt}\right)_M = -\frac{1}{\rho}\vec{\nabla}\cdot\vec{q} \tag{A.8}$$

Here, q denotes the outward heat flux, under the assumption that there is no inward flux. In the spherically symmetric case, substituting Equation (2.18) yields

$$T\left(\frac{\partial s}{\partial t}\right)_M = -\frac{1}{4\pi\rho r^2}\frac{\partial L}{\partial r} \tag{A.9}$$

The first law of thermodynamics can be written as

$$dU = TdS - pdV \tag{A.10}$$

Here, s is the entropy and u is the specific internal energy, the latter being defined as

$$u = \frac{3}{2}\frac{k_B T}{m} \tag{A.11}$$

Solving equation (A.10) for ds and integrating gives

$$s = \frac{k_B}{T} ln\left(\frac{T^{3/2}}{\rho}\right) \tag{A.12}$$

Substituting (A.12) into (A.9) and using $\nu^2 = k_B T/m$ yields

$$\frac{\partial L}{\partial r} = -4\pi\rho r^2\nu^2\left(\frac{\partial}{\partial t}\right)_M ln\frac{\nu^3}{\rho} \tag{A.13}$$

Appendix B

Methodological Supplements

B.1 Testing the code with the results from Ref. [71]

To validate the correctness of the applied methodology, the results of [71] were reproduced as a first step. A comparison is shown in Fig.B.1 (Power Spectrum as a function of ϕ_1) and Fig.B.2 (Power Spectrum as a function of s). It can be seen that the results of [71] were largely reproduced. In both cases, the shape of the spectrum closely matches the original result, and in particular, the peak at $1/k_s = 2.64 \pm 0.18\,\mathrm{kpc}$ is clearly visible, which was the key finding in the analysis by [71]. The deviations in both spectra are of comparable magnitude. In the case of the power spectrum as a function of s, it must be noted that, due to the lack of precise data, the positions of the stars within each bin were assigned randomly during the computation. This is a likely explanation for minor discrepancies. The source of the differences in the power spectrum as a function of ϕ_1 is less clear; they may result from slight differences in the underlying dataset. Nevertheless, the result could be reproduced in its main structure.

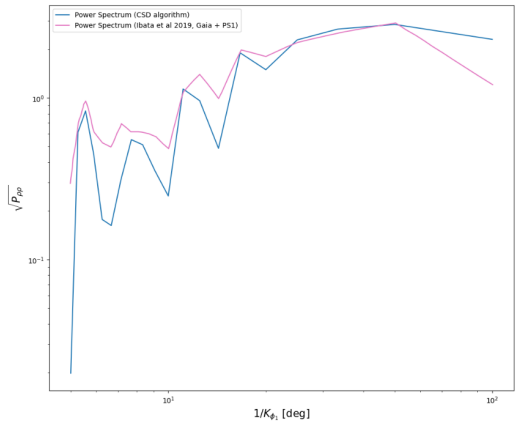

FIGURE B.1: Power Spectrum as a function of ϕ_1 (blue) and comparison with the results from [71] (purple).

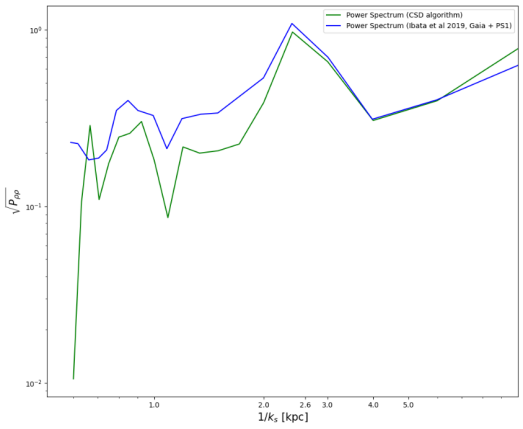

FIGURE B.2: Power Spectrum as a function of s (green) and comparison with the results from [71] (blue).

Acknowledgements

First and foremost, I would like to express my deepest gratitude to Prof. Laura Sagunski for welcoming me into her group. Thanks to her, I had the opportunity not only to explore some of the most fascinating questions in the universe, but also to take part in great experiences such as the Explore project and a trip to Canada. I am also deeply grateful for her kind and empathetic nature, which made me feel comfortable and supported at all times.

I would also like to sincerely thank Prof. Sean Tulin. Working with him as part of the Stream Team was always a great pleasure, and I particularly appreciated his personal visit to Frankfurt last summer.

My sincere thanks also go to Prof. Jürgen Schaffner-Bielich for kindly agreeing to serve as second examiner. I remember many pleasant encounters with great joy.

I am also very grateful to all members of the research group for the great atmosphere and many sources of inspiration. In particular, I would like to thank Edwin Genoux-Prachex for many enjoyable hours in the office, great conversations on a wide range of topics, his generous help with programming, proofreading of the thesis, and for answering many questions about the universe.

I would like to thank everyone who has given me love, support, joy, and passion during the last months and years.

Most of all, I would like to thank my family, especially my mother, whose constant support and love mean everything to me.

Bibliography

[1] G. Aad, T. Abajyan, and B. Abbott et al. Observation of a new particle in the search for the standard model higgs boson with the atlas detector at the lhc. *Physics Letters B*, 716(1):1–29, September 2012.

[2] James Adams et al. Semi-analytical predictions of subhalo-induced features in gd-1-like streams, 2024.

[3] P. A. R. Ade, N. Aghanim, and M. et al. Arnaud. Planck2015 results: Xiii. cosmological parameters. *Astronomy amp; Astrophysics*, 594:A13, September 2016.

[4] Tarnem Afify, Reuben Blaff, Charlotte Bordt, Nassim Bozorgnia, Alexander Huhn, Benjamin Mendez, Elham Rahimi, Laura Sagunski, Sean Tulin, and Hannah Vormann. Stellar stream tests of dark matter cores, cusps, and super-cusps. Manuscript in preparation, July 2025.

[5] Hirotogu Akaike. Power spectrum estimation through autoregressive model fitting. *AISM*, 21:407 – 419, December 1969.

[6] Astropy Collaboration. Astropy: A community python package for astronomy. https://www.astropy.org/, 2025. Accessed: 2025-07-23.

[7] Maurice J. Bach. *The Design of the UNIX Operating System*. Prentice Hall, Englewood Cliffs, NJ, 1986.

[8] Neta A. Bahcall, Jeremiah P. Ostriker, Saul Perlmutter, and Paul J. Steinhardt. The cosmic triangle: Revealing the state of the universe. *Science*, 284(5419):1481–1488, May 1999.

[9] Shmuel Balberg, Stuart L. Shapiro, and Shogo Inagaki. Self-interacting dark matter halos and the gravothermal catastrophe. *The Astrophysical Journal*, 568(2):475–487, April 2002.

[10] Nilanjan Banik and Jo Bovy. Effects of baryonic and dark matter substructure on the pal 5 stream. *Monthly Notices of the Royal Astronomical Society*, 484(2):2009–2020, January 2019.

[11] M.S. Bartlett. Smoothing Periodograms from Time-Series with Continuous Spectra. *Nature*, 161:686–687, May 1948.

[12] H Baumgardt and E Vasiliev. Accurate distances to galactic globular clusters through a combination of gaia edr3, hst, and literature data. *Monthly Notices of the Royal Astronomical Society*, 505(4):5957–5977, May 2021.

[13] Edouard J. et al. Bernard. Stellar streams discovered in the pan-starrs1 3 survey. *Monthly Notices of the Royal Astronomical Society*, 463(2):1759–1774, 2016.

[14] Gianfranco Bertone, Dan Hooper, and Joseph Silk. Particle dark matter: evidence, candidates and constraints. *Physics Reports*, 405(5–6):279–390, January 2005.

[15] James Binney and Scott Tremaine. *Galactic Dynamics*. Princeton University Press, 2nd edition, 2008.

[16] Joss Bland-Hawthorn and Ortwin Gerhard. The galaxy in context: Structural, kinematic, and integrated properties. *Annual Review of Astronomy and Astrophysics*, 54(Volume 54, 2016):529–596, August 2016.

[17] Ana Bonaca, Charlie Conroy, Adrian M. Price-Whelan, and David W. Hogg. Multiple components of the jhelum stellar stream. *The Astrophysical Journal Letters*, 881(2):L37, August 2019.

[18] Ana Bonaca and David W. Hogg. The information content in cold stellar streams. *The Astrophysical Journal*, 867(2):101, November 2018.

[19] Ana Bonaca, David W. Hogg, Adrian M. Price-Whelan, and Charlie Conroy. The spur and the gap in gd-1: Dynamical evidence for a dark substructure in the milky way halo. *The Astrophysical Journal*, 880(1):38, July 2019.

[20] Ana Bonaca, David W. Hogg, Adrian M. Price-Whelan, and Charlie Conroy. Radial velocity dispersion of gd-1 and implications for dark matter substructure. *Astrophysical Journal*, 889(2):71, November 2020.

[21] Ana Bonaca and Adrian M. Price-Whelan. Stellar streams in the gaia era, 2024.

[22] J. R. Bond, G. Efstathiou, and J. Silk. Massive neutrinos and the large-scale structure of the universe. *Phys. Rev. Lett.*, 45:1980–1984, December 1980.

[23] J. Richard Bond, Alex S. Szalay, and Michael S. Turner. Formation of galaxies in a neutrino-dominated universe. *Physical Review Letters*, 48(9):1636–1639, June 1982.

[24] Charlotte Clara Bordt. Studies of self-interacting dark matter: An extension of the jeans formalism and a search for the gd-1 perturber. Master's thesis, Institute for Theoretical Physics, Goethe University Frankfurt, Frankfurt am Main, Germany,

March 2023. Supervisors: Prof. Dr. Laura Sagunski and Prof. Dr. Jürgen Schaffner-Bielich.

[25] Jo Bovy, Anita Bahmanyar, Tobias K. Fritz, and Nitya Kallivayalil. The shape of the inner milky way halo from observations of the pal 5 and gd–1 stellar streams. *The Astrophysical Journal*, 833(1):31, December 2016.

[26] Jo Bovy, Denis Erkal, and Jason L. Sanders. Linear perturbation theory for tidal streams and the small-scale cdm power spectrum. *Monthly Notices of the Royal Astronomical Society*, 466(1):628–668, November 2016.

[27] Jo Bovy, Denis Erkal, and Jason L. Sanders. Linear perturbation theory for tidal streams and the small-scale cdm power spectrum. *Monthly Notices of the Royal Astronomical Society*, 466(1):628–668, November 2016.

[28] Michael Boylan-Kolchin, James S. Bullock, and Manoj Kaplinghat. The milky way's bright satellites as an apparent failure of cdm: The mw's bright satellites in cdm. *Monthly Notices of the Royal Astronomical Society*, 422(2):1203–1218, March 2012.

[29] Ronald N. Bracewell. *The Fourier Transform and Its Applications*. McGraw-Hill, New York, 3 edition, 2000.

[30] J. R. Brownstein and J. W. Moffat. The bullet cluster 1e0657-558 evidence shows modified gravity in the absence of dark matter. *Monthly Notices of the Royal Astronomical Society*, 382(1):29–47, November 2007.

[31] Greg L. Bryan and Michael L. Norman. Statistical properties of x-ray clusters: Analytic and numerical comparisons. *The Astrophysical Journal*, 495:80–99, March 1998.

[32] James S. Bullock and Michael Boylan-Kolchin. Small-scale challenges to the cdm paradigm. *Annual Review of Astronomy and Astrophysics*, 55(1):343–387, August 2017.

[33] R. G. Carlberg and C. J. Grillmair. Quantifying gaps in the gd-1 stellar stream: evidence for dark matter subhalos. *Astrophysical Journal*, 768(2):171, April 2013.

[34] Raymond G. Carlberg. Gd-1 and the milky way starless subhalos, 2025.

[35] Raymond G. Carlberg, Adrian Jenkins, Carlos S. Frenk, and Andrew P. Cooper. Star stream velocity distributions in cdm and wdm galactic halos, 2024.

[36] Bernard Carr, Florian Kühnel, and Marit Sandstad. Primordial black holes as dark matter. *Phys. Rev. D*, 94:083504, October 2016.

[37] S. Chandrasekhar. Dynamical friction. i. general considerations: The coefficient of dynamical friction. *The Astrophysical Journal*, 97:255–262, March 1943.

[38] Douglas Clowe, Maruša Bradač, Anthony H. Gonzalez, Maxim Markevitch, Scott W. Randall, Christine Jones, and Dennis Zaritsky. A direct empirical proof of the existence of dark matter. *The Astrophysical Journal*, 648(2):L109–L113, August 2006.

[39] Gaia Collaboration. Gaia data release 1. *Astronomy Astrophysics*, 595:A1, November 2016.

[40] Even Coquery and Alain Blanchard. Cosmological implications of the gaia milky way declining rotation curve, 2024.

[41] E. Corbelli and P. Salucci. The extended rotation curve and the dark matter halo of m33. *Monthly Notices of the Royal Astronomical Society*, 311(2):441–447, January 2000.

[42] Lyman Lab. of Physics Cornell University. Elementary particle physics – applications of quantum mechanics lecture. Online lecture notes, 2025. Accessed: 2025-07-20.

[43] Romeel Dave, David N. Spergel, Paul J. Steinhardt, and Benjamin D. Wandelt. Halo properties in cosmological simulations of self-interacting cold dark matter. *The Astrophysical Journal*, 547(2):574–589, February 2001.

[44] Marc Davis, George Efstathiou, Carlos S Frenk, and Simon D M White. The evolution of large-scale structure in a universe dominated by cold dark matter. *The Astrophysical Journal*, 292:371–394, June 1985.

[45] T J L de Boer, V Belokurov, S E Koposov, L Ferrarese, D Erkal, P Côté, and J F Navarro. A deeper look at the gd1 stream: density variations and wiggles. *Monthly Notices of the Royal Astronomical Society*, 477(2):1893–1902, March 2018.

[46] T.J.L. de Boer, Vasily A Belokurov, Sergey E. Koposov, Laura Ferrarese, Denis Erkal, Patrick Côté, and Julio F. Navarro. A deeper look at the gd1 stream: density variations and wiggles. *Monthly Notices of the Royal Astronomical Society*, 477:1893–1902, January 2018.

[47] A. Del Popolo. Dark matter, density perturbations, and structure formation. *Astronomy Reports*, 51(3):169–196, March 2007.

[48] P. A. M. Dirac. The quantum theory of the electron. *Proceedings of the Royal Society of London. Series A, Containing Papers of a Mathematical and Physical Character*, 117(778):610–624, February 1928.

[49] A. Drlica-Wagner, K. Bechtol, E. S. Rykoff, and et al. Eight ultra-faint galaxy candidates discovered in year two of the dark energy survey. *The Astrophysical Journal*, 813(2):109, November 2015.

[50] John Dubinski and R. G. Carlberg. The structure of cold dark matter halos. , 378:496, September 1991.

[51] Ruth Durrer. The cosmic microwave background: the history of its experimental investigation and its significance for cosmology. *Classical and Quantum Gravity*, 32(12):124007, June 2015.

[52] Aaron A. Dutton and Andrea V. Macciò. Cold dark matter haloes in the planck era: evolution of structural parameters for einasto and nfw profiles. *Monthly Notices of the Royal Astronomical Society*, 441(4):3359–3374, May 2014.

[53] Jaan Einasto. On the construction of a composite model for the galaxy and on the determination of the system of galactic parameters. *Trudy Astrofizicheskogo Instituta Alma-Ata*, 5:87, January 1965.

[54] Oliver D. Elbert, James S. Bullock, Shea Garrison-Kimmel, Miguel Rocha, Jose Oñorbe, and Annika H. G. Peter. Core formation in dwarf haloes with self-interacting dark matter: no fine-tuning necessary. *Monthly Notices of the Royal Astronomical Society*, 453(1):29–37, August 2015.

[55] Denis Erkal. A sharper view of pal 5's tails: discovery of stream perturbations with a novel non-parametric technique. *Monthly Notices of the Royal Astronomical Society*, 470(1):60–84, May 2017.

[56] Denis Erkal, Sergey E. Koposov, and Vasily Belokurov. A sharper view of pal 5's tails: discovery of stream perturbations with a novel non-parametric technique. *Monthly Notices of the Royal Astronomical Society*, 470(1):60–84, May 2017.

[57] Donald G. York et al. The sloan digital sky survey: Technical summary. *The Astronomical Journal*, 120:1579–1587, June 2000.

[58] European Southern Observatory (ESO). Artistic illustration of a wormhole, 2025.

[59] Jonathan L. Feng. Dark matter candidates from particle physics and methods of detection. *Annual Review of Astronomy and Astrophysics*, 48(1):495–545, August 2010.

[60] R. Foot and S. Vagnozzi. Dissipative hidden sector dark matter. *Physical Review D*, 91(2), January 2015.

[61] Message P Forum. *MPI: A Message-Passing Interface Standard*. University of Tennessee, USA, April 1994.

[62] H. Fritzsch, M. Gell-Mann, and H. Leutwyler. Advantages of the color octet gluon picture. *Physics Letters B*, 47(4):365–368, November 1973.

[63] Katherine Garrett and Gintaras Duda. Dark matter: A primer. *Advances in Astronomy*, 2011:1–22, January 2011.

[64] Sheridan B Green and Frank C van den Bosch. The tidal evolution of dark matter substructure – i. subhalo density profiles. *Monthly Notices of the Royal Astronomical Society*, 490(2):2091–2101, October 2019.

[65] C. J. Grillmair and O. Dionatos. Detection of a 63° cold stellar stream in the sloan digital sky survey. *The Astrophysical Journal*, 643(1):L17, May 2006.

[66] Fredric J. Harris. On the use of windows for harmonic analysis with the discrete fourier transform. *Proceedings of the IEEE*, 66(1):51–83, January 1978.

[67] Philip Harris, Philip Schuster, and Jure Zupan. Snowmass white paper: New flavors and rich structures in dark sectors, 2022.

[68] Amina Helmi. The stellar halo of the galaxy. *The Astronomy and Astrophysics Review*, 15(3):145–188, April 2008.

[69] Lars Hernquist. An Analytical Model for Spherical Galaxies and Bulges. , 356:359, June 1990.

[70] P. W. Hodge. The Hubble type of the Milky Way Galaxy. , 95:721–723, October 1983.

[71] Rodrigo A. Ibata, Khyati Malhan, and Nicolas F. Martin. The streams of the gaping abyss: A population of entangled stellar streams surrounding the inner galaxy. *The Astrophysical Journal*, 872(2):152, February 2019.

[72] Austin Joyce, Bhuvnesh Jain, Justin Khoury, and Mark Trodden. Beyond the cosmological standard model. *Physics Reports*, 568:1–98, March 2015.

[73] G. Kauffmann, S. D. M. White, and B. Guiderdoni. The formation and evolution of galaxies within merging dark matter haloes. , 264:201–218, September 1993.

[74] Anatoly Klypin, Andrey V. Kravtsov, Octavio Valenzuela, and Francisco Prada. Where are the missing galactic satellites? *The Astrophysical Journal*, 522(1):82–92, September 1999.

[75] C. S. Kochanek and Martin White. A quantitative study of interacting dark matter in halos. *The Astrophysical Journal*, 543(2):514–520, November 2000.

[76] Sergey E. Koposov, Hans-Walter Rix, and David W. Hogg. Constraining the milky way potential with a six-dimensional phase-space map of the gd-1 stellar stream. *The Astrophysical Journal*, 712(1):260–273, February 2010.

[77] Andreas H. W. Küpper, Andrew Macleod, and Douglas C. Heggie. On the structure of tidal tails. *Monthly Notices of the Royal Astronomical Society*, 387(3):1248–1252, July 2008.

[78] C. Lacey and S. Cole. Merger rates in hierarchical models of galaxy formation. *Monthly Notices of the Royal Astronomical Society*, 262:627–649, June 1993.

[79] B. W. Lee and S. Weinberg. Cosmological lower bound on heavy neutrino masses. *Physical Review Letters*, 39(4):165–168, July 1977.

[80] Pathma Liyanage. Cdm theory, the constituents of the universe and the growth of structures: A review, 12 2020.

[81] Avi Loeb. Interstellar interpretation of plato's cave allegory. https://avi-loeb.medium.com/interstellar-interpretation-of-platos-cave-allegory-b74f24b1a5c, March 2023. Accessed: 2025-07-19.

[82] Mark Lutz. *Programming Python*. O'Reilly Media, 4 edition, 2011.

[83] Khyati Malhan and Rodrigo A Ibata. Constraining the milky way halo potential with the gd-1 stellar stream. *Monthly Notices of the Royal Astronomical Society*, 486(3):2995–3005, April 2019.

[84] Khyati Malhan and Rodrigo A Ibata. Constraining the milky way halo potential with the gd-1 stellar stream. *Monthly Notices of the Royal Astronomical Society*, 486(3):2995–3005, April 2019.

[85] M. Markevitch, A. H. Gonzalez, D. Clowe, A. Vikhlinin, W. Forman, C. Jones, S. Murray, and W. Tucker. Direct constraints on the dark matter self-interaction cross section from the merging galaxy cluster 1e 065756. *The Astrophysical Journal*, 606(2):819–824, May 2004.

[86] Charles W. Misner, Kip S. Thorne, and John Archibald Wheeler. *Gravitation*. W. H. Freeman and Company, San Francisco, 1st edition, 1973.

[87] M. Miyamoto and R. Nagai. Three-dimensional models for the distribution of mass in galaxies. , 27:533–543, January 1975.

[88] B. Moore, T. Quinn, F. Governato, J. Stadel, and G. Lake. Cold collapse and the core catastrophe. *Monthly Notices of the Royal Astronomical Society*, 310(4):1147–1152, December 1999.

[89] Ben Moore. Evidence against dissipation-less dark matter from observations of galaxy haloes. , 370(6491):629–631, August 1994.

[90] Ben Moore, Sebastiano Ghigna, Fabio Governato, George Lake, Thomas Quinn, Joachim Stadel, and Paolo Tozzi. Dark matter substructure within galactic halos. *The Astrophysical Journal*, 524(1):L19–L22, October 1999.

[91] Michael S. Morris, Kip S. Thorne, and Ulvi Yurtsever. Wormholes, time machines, and the weak energy condition. *Physical Review Letters*, 61(13):1446–1449, September 1988.

[92] Julio F. Navarro, Carlos S. Frenk, and Simon D. M. White. The assembly of galaxies in a hierarchically clustering universe. *Monthly Notices of the Royal Astronomical Society*, 275(1):56–66, July 1995.

[93] Julio F. Navarro, Carlos S. Frenk, and Simon D. M. White. The structure of cold dark matter halos. *The Astrophysical Journal*, 462:563, May 1996.

[94] Julio F. Navarro, Carlos S. Frenk, and Simon D. M. White. A universal density profile from hierarchical clustering. *The Astrophysical Journal*, 490(2):493–508, December 1997.

[95] H. Nyquist. Certain topics in telegraph transmission theory. *Transactions of the American Institute of Electrical Engineers*, 47(2):617–644, April 1928.

[96] Kyle A. Oman, Julio F. Navarro, Azadeh Fattahi, Carlos S. Frenk, Till Sawala, Simon D. M. White, Richard Bower, Robert A. Crain, Michelle Furlong, Matthieu Schaller, Joop Schaye, and Tom Theuns. The unexpected diversity of dwarf galaxy rotation curves. *Monthly Notices of the Royal Astronomical Society*, 452(4):3650–3665, August 2015.

[97] Alan V. Oppenheim and Ronald W. Schafer. *Discrete-Time Signal Processing*. Prentice Hall, Upper Saddle River, NJ, 3 edition, 2010.

[98] Carles G Palau and Jordi Miralda-Escudé. The oblateness of the milky way dark matter halo from the stellar streams of ngc 3201, m68, and palomar 5. *Monthly Notices of the Royal Astronomical Society*, 524(2):2124–2147, June 2023.

[99] Jeffrey M Patrick, Sergey E Koposov, and Matthew G Walker. Uniform modelling of the stellar density of thirteen tidal streams within the galactic halo. *Monthly Notices of the Royal Astronomical Society*, 514(2):1757–1781, May 2022.

[100] Sarah Pearson, Andreas H. W. Küpper, Kathryn V. Johnston, and Adrian M. Price-Whelan. Tidal stream morphology as an indicator of dark matter halo geometry: The case of palomar 5. *The Astrophysical Journal*, 799(1):28, January 2015.

[101] P. J. E. Peebles. *The Large-Scale Structure of the Universe*. Princeton University Press, 1980.

[102] P. J. E. Peebles and Bharat Ratra. The cosmological constant and dark energy. *Reviews of Modern Physics*, 75(2):559–606, April 2003.

[103] A. A. Penzias and R. W. Wilson. A Measurement of Excess Antenna Temperature at 4080 Mc/s. , 142:419–421, July 1965.

[104] Annika H. G. Peter, Miguel Rocha, James S. Bullock, and Manoj Kaplinghat. Cosmological simulations with self-interacting dark matter – ii. halo shapes versus observations. *Monthly Notices of the Royal Astronomical Society*, 430(1):105–120, January 2013.

[105] Adrian M. Price-Whelan and Ana Bonaca. Off the beaten path: Gaia reveals gd-1 stars outside of the main stream. *The Astrophysical Journal Letters*, 863(2):L20, August 2018.

[106] Joel R. Primack. Cosmological structure formation, 2015.

[107] Python Software Foundation. What is python? executive summary. https://www.python.org/doc/essays/blurb/, 2024. Accessed: 2025-07-23.

[108] V. C. Rubin, W. K. Ford, Jr., and N. Thonnard. Rotational properties of 21 SC galaxies with a large range of luminosities and radii, from NGC 4605 (R=4kpc) to UGC 2885 (R=122kpc). , 238:471–487, June 1980.

[109] Vera C. Rubin and W. Kent Ford, Jr. Rotation of the Andromeda Nebula from a Spectroscopic Survey of Emission Regions. , 159:379, February 1970.

[110] Varun Sahni. *5 Dark Matter and Dark Energy*, page 141–179. Springer Berlin Heidelberg, December 2004.

[111] Allan Sandage. *The Hubble Atlas of Galaxies*. Carnegie Institution of Washington, Washington, D.C., 1986.

[112] Arthur Schuster. On the investigation of hidden periodicities with application to a supposed 26 day period of meteorological phenomena. *Terrestrial Magnetism*, 3(1):13, January 1898.

[113] Masato Shirasaki, Takashi Okamoto, and Shin'ichiro Ando. Modelling self-interacting dark matter substructures – i. calibration with n-body simulations of a milky-way-sized halo and its satellite. *Monthly Notices of the Royal Astronomical Society*, 516(3):4594–4611, September 2022.

[114] Jannis Simon. The influence of self-interacting dark matter halos with elastic and inelastic scattering on tidal streams. Master's thesis, Goethe University Frankfurt am Main, Frankfurt am Main, Germany, March 2024. Supervisors: Prof. Dr. Ulrich Achatz and Prof. Dr. Laura Sagunski.

[115] Joshua D. Simon and Marla Geha. The kinematics of the ultra-faint milky way satellites: Solving the missing satellite problem. *The Astrophysical Journal*, 670(1):313–331, November 2007.

[116] SLURM Team. Slurm workload manager overview. `https://slurm.schedmd.com/overview.html`, 2025. Accessed: 2025-07-23.

[117] D. N. Spergel, L. Verde, H. V. Peiris, E. Komatsu, M. R. Nolta, C. L. Bennett, M. Halpern, G. Hinshaw, N. Jarosik, A. Kogut, M. Limon, S. S. Meyer, L. Page, G. S. Tucker, J. L. Weiland, E. Wollack, and E. L. Wright. First-year wilkinson microwave anisotropy probe (wmap) observations: Determination of cosmological parameters. *The Astrophysical Journal Supplement Series*, 148(1):175–194, September 2003.

[118] David N. Spergel and Paul J. Steinhardt. Observational evidence for self-interacting cold dark matter. *Physical Review Letters*, 84(17):3760–3763, April 2000.

[119] V. Springel, J. Wang, M. Vogelsberger, A. Ludlow, A. Jenkins, A. Helmi, J. F. Navarro, C. S. Frenk, and S. D. M. White. The aquarius project: the subhaloes of galactic haloes. *Monthly Notices of the Royal Astronomical Society*, 391(4):1685–1711, December 2008.

[120] Volker Springel, Carlos S. Frenk, and Simon D. M. White. The large-scale structure of the universe. *Nature*, 440(7088):1137–1144, April 2006.

[121] Volker Springel and Lars Hernquist. The history of star formation in a cold dark matter universe. *Monthly Notices of the Royal Astronomical Society*, 339(2):312–334, February 2003.

[122] Volker Springel, Simon D. M. White, Adrian Jenkins, Carlos S. Frenk, Naoki Yoshida, Liang Gao, Julio Navarro, Robert Thacker, Darren Croton, John Helly, John A. Peacock, Shaun Cole, Peter Thomas, Hugh Couchman, August Evrard,

Jörg Colberg, and Frazer Pearce. Simulations of the formation, evolution and clustering of galaxies and quasars. *Nature*, 435(7042):629–636, June 2005.

[123] Petre Stoica and Randolph L. Moses. *Spectral Analysis of Signals*. Prentice Hall, Upper Saddle River, NJ, 1 edition, 2005.

[124] Max Tegmark. Cmb mapping experiments: A designer's guide. *Physical Review D*, 56(8):4514–4529, October 1997.

[125] David Thomson. Spectrum estimation and harmonic analysis. *Proceedings of the IEEE*, 70:1055 – 1096, October 1982.

[126] M. Tristram, A. J. Banday, M. Douspis, X. Garrido, K. M. Górski, S. Henrot-Versillé, L. T. Hergt, S. Ilić, R. Keskitalo, G. Lagache, C. R. Lawrence, B. Partridge, and D. Scott. Cosmological parameters derived from the final planck data release (pr4). *Astronomy amp; Astrophysics*, 682:A37, January 2024.

[127] Sean Tulin and Hai-Bo Yu. Dark matter self-interactions and small scale structure. *Physics Reports*, 730:1–57, February 2018.

[128] J. A. Tyson, F. Valdes, and R. A. Wenk. Detection of Systematic Gravitational Lens Galaxy Image Alignments: Mapping Dark Matter in Galaxy Clusters. , 349:L1, January 1990.

[129] Sidney van den Bergh. *The Galaxies of the Local Group*. Cambridge University Press, Cambridge, UK, 1999.

[130] Sidney Van Den Bergh. Globular clusters and dwarf spheroidal galaxies. *Monthly Notices of the Royal Astronomical Society: Letters*, 385(1):L20–L22, March 2008.

[131] Pauli Virtanen, Ralf Gommers, Travis Oliphant, Matt Haberland, Tyler Reddy, David Cournapeau, Evgeni Burovski, Pearu Peterson, Warren Weckesser, Jonathan Bright, Stéfan Walt, Matthew Brett, Joshua Wilson, K. Millman, Nikolay Mayorov, Andrew Nelson, Eric Jones, Robert Kern, Eric Larson, and Yoshiki Vázquez-Baeza. Scipy 1.0: fundamental algorithms for scientific computing in python. *Nature Methods*, 17:1–12, February 2020.

[132] Mark Vogelsberger, Jesus Zavala, and Abraham Loeb. Subhaloes in self-interacting galactic dark matter haloes: Self-interacting galactic dark matter haloes. *Monthly Notices of the Royal Astronomical Society*, 423(4):3740–3752, May 2012.

[133] Steven Weinberg. *Cosmology*. Oxford University Press, Oxford, UK, 2008.

[134] P. Welch. The use of fast fourier transform for the estimation of power spectra: A method based on time averaging over short, modified periodograms. *IEEE Transactions on Audio and Electroacoustics*, 15(2):70–73, June 1967.

[135] Xin Xu, Hu Zou, Xu Zhou, Jundan Nie, Zhimin Zhou, Jun Ma, Tianmeng Zhang, Jiali Wang, and Suijian Xue. New determination of fundamental properties of palomar 5 using deep desi imaging data. *The Astronomical Journal*, 161(1):12, December 2020.

[136] F. Zwicky. Die Rotverschiebung von extragalaktischen Nebeln. *Helvetica Physica Acta*, 6:110–127, January 1933.

[137] F. Zwicky. On the Masses of Nebulae and of Clusters of Nebulae. , 86:217, October 1937.